

Aquatic and Crop Resource Development
Bio-based Specialty Chemicals Program

NRC-CNRC

Characterization of Snow Crab Shells

For: Renée Allain, MSc. - Fisheries and Oceans Canada

NRC Contributors: Aïssa Harhira, Maxime Rivard, Guy Lamouche, André Beauchesne, Silvio Kruger, Josette El Haddad, David Rocheleau, and Alain Blouin

Document Number: A1-012097-R1

Date: December 21, 2017

Protected B Confidential



National Research
Council Canada

Conseil national de
recherches Canada

Canada 

Contents

| | |
|--|----|
| List of figures | 3 |
| List of tables..... | 5 |
| 1. Introduction | 6 |
| 2. Objectives | 6 |
| 3. Samples Description | 7 |
| 4. LIBS Measurements | 7 |
| 4.1 Experimental..... | 7 |
| 4.2 Measurements..... | 8 |
| 4.3 Results..... | 9 |
| 5. OCT Measurements..... | 22 |
| 5.1 Experimental..... | 22 |
| 5.2 Measurements..... | 23 |
| 5.3 Results..... | 24 |
| 6. Ultrasounds Measurements | 35 |
| 6.1 Experimental..... | 35 |
| 6.2 Measurements..... | 35 |
| 6.3 Results..... | 37 |
| 7. Conclusions and recommendations | 40 |
| 8. References | 42 |

List of figures

| | |
|--|----|
| Figure 1 : LIBS experimental setup | 8 |
| Figure 2 : LIBS spectra of dorsal carapace (Si from marine sand is shown in the spectra acquired by the first 200 laser shots)..... | 9 |
| Figure 3 : LIBS spectra in different spectral ranges (a) 250-250 nm, (b) 350–430 nm and (c) 500–850 nm..... | 11 |
| Figure 4 : Depth profiling of Mg(II)/Mg(I) ratios in chelipeds of different snow crabs..... | 13 |
| Figure 5 : Depth profiling of Mg/Ca ratios in chelipeds of different snow crabs..... | 13 |
| Figure 6 : Averaged Mg/Ca ratios in chelipeds for different snow crabs | 14 |
| Figure 7 : Depth profiling of Mg(II)/Mg(I) ratios in carapace dorsal of different snow crabs..... | 14 |
| Figure 8 Laser ablation marks on crab #4 (left) and crab #5 (right) | 15 |
| Figure 9 : Averaged Mg/Ca ratios in carapaces for different snow crabs..... | 15 |
| Figure 10 : Ablation mark on merus of crab #2..... | 16 |
| Figure 11 : Depth profiling of Mg(II)/Mg(I) ratios in merus of different snow crabs | 16 |
| Figure 12 : Averaged Mg(II)/Mg(I) ratios in merus for different snow crabs | 17 |
| Figure 13 : Averaged Mg/Ca ratios in merus for different snow crabs | 17 |
| Figure 14 : PCA score plot of cheliped LIBS spectra. The legend includes the moulting condition. | 18 |
| Figure 15 : PCA loadings plot of cheliped LIBS spectra. | 19 |
| Figure 16 : PCA score plot of dorsal carapace LIBS spectra. The legend includes the moulting condition. | 19 |
| Figure 17 : PCA score plot of merus spectra. The legend includes the moulting condition. | 20 |
| Figure 18 : PCA loading plot of merus spectra. | 20 |
| Figure 19 : Swept-source OCT system..... | 23 |
| Figure 20 : Optical scanner and crab sample. | 23 |
| Figure 21 : (a) Top of crab #1 carapace. (b, c) OCT tomographic reconstructions. | 24 |
| Figure 22 : (a) Bottom of crab #1 carapace. (b, c) OCT tomographic reconstructions. | 25 |
| Figure 23 : (a) Tomographic reconstruction of (b) the cheliped of crab #4 (condition 2). (c, d) B-Scan reconstruction in the red and green planes of a) showing the shell thickness..... | 26 |
| Figure 24 : (a) Tomographic reconstruction of the cheliped of crab #5 (condition 3). (b, c) B-Scan reconstruction in the red and green planes of a) showing the shell thickness..... | 27 |
| Figure 25 : (a) Tomographic reconstruction of the cheliped of crab #3 (condition 4). (b, c) B-Scan reconstruction in the red and green planes of a) showing the shell thickness..... | 28 |

| | |
|--|----|
| Figure 26 : (a) Tomographic reconstruction of (d) the carapace intestinal region of crab #4 (condition 2). (b, c) B-Scan reconstruction in the green and red planes of a) showing the shell thickness..... | 29 |
| Figure 27 : (a) Tomographic reconstruction of (d) the carapace intestinal region of crab #5 (condition 3). (b, c) B-Scan reconstruction in the green and red planes of a) showing the shell thickness..... | 29 |
| Figure 28 : (a) Tomographic reconstruction of the carapace intestinal region of crab #3 (condition 4). (b, c) B-Scan reconstruction in the green and red planes of a) showing the shell thickness..... | 30 |
| Figure 29 : (a) Tomographic reconstruction of (b) the merus of crab #4 (condition 2). (c, d) B-Scan reconstruction in the red and green planes of a) showing the shell thickness..... | 31 |
| Figure 30 : (a) Tomographic reconstruction of (d) the merus of crab #5 (condition 3). (b, c) B-Scan reconstruction in the red and green planes of a) showing the shell thickness..... | 31 |
| Figure 31 : (a) Tomographic reconstruction of the merus of crab #3 (condition 4). (b, c) B-Scan reconstruction in the red and green planes of a) showing the shell thickness..... | 32 |
| Figure 32 : (a, b) Tomographic reconstruction of the merus of crab #2 (condition 3M). (c, d) B-Scan reconstruction in the red and blue planes of a) showing the shell thickness. | 33 |
| Figure 33 : (a) Tomographic reconstruction of the merus of crab #3 (condition 4). (b, c) B-Scan reconstruction in the red and blue planes of a) showing the shell thickness. | 34 |
| Figure 34 : (a) Schematic view of the ultrasonic transducer and the multiple echoes coming from the interfaces and (b) picture of the testing the merus of the 2nd pereopod. | 35 |
| Figure 35 : Signal measured only with the delay line. Horizontal axis is the time in μ s and the vertical axis is the signal amplitude. | 36 |
| Figure 36 : Signal measured in the merus of the 2nd pereopod of crab #3..... | 36 |
| Figure 37 : Signal measured in the merus of the 2nd pereopod of crab #3 in other position than that shown in Figure 36..... | 37 |
| Figure 38 : Ultrasonic signals obtained on Cheliped of Chela from the tested crabs. | 38 |
| Figure 39 : Ultrasonic signals obtained on Merus of the 2nd pereopod from the tested crabs. ... | 38 |

List of tables

| | |
|---|----|
| Table 1 : Snow crabs characteristics..... | 7 |
| Table 2 : Main emission lines detected by LIBS in snow crabs..... | 10 |

1. Introduction

Like all crustaceans, snow crabs go through a process of moulting to allow them to grow. In this process, the hard shell is shed and a new soft shell is generated and essentially filled with water prior to mineralization, thus allowing room for the crustaceans to grow. Unlike lobsters, snow crab will undergo a terminal or final moult once they reach maturity. As such, the Fisheries and Oceans Department (DFO) is interested in determining if National Research Council (NRC) technologies may be useful in determining the properties of snow crab shells and distinguishing “moulters” from “terminal-moulters”.

2. Objectives

The main objective is to explore the applicability of three techniques to characterize snow crab shells in order to distinguish different moulting stages.

The three techniques are:

1. Laser Induced Breakdown Spectroscopy (LIBS).
2. Optical Coherence Tomography (OCT).
3. Ultrasonic measurements.

For the LIBS evaluation, this project tasks are focused on the detection and the determination of chemical elements forming the shell in order to determine the properties of the moult. NRC will determine the feasibility of making LIBS measurements on the shell. Moreover, NRC will evaluate the use of chemometrics coupled to LIBS to distinguish variability between snow crabs having different moulting stages.

For OCT, the tasks are focused on assessing the capability of OCT to perform tomographic measurements through the shell. A through-shell measurement should not only allow for the measurement the shell thickness, but to also observe the internal structure of the shell.

For ultrasonic measurements, NRC will explore the opportunities for characterization of snow crab shell. Measurements will be performed to determine which conditions (frequency, transmission or pulse-echo, etc.) ultrasound can propagate through the shell.

3. Samples Description

DFO provided NRC with six frozen snow crabs which have reached different moulting stages. Table 1 summarizes sample details such as the moulting stage, dimensions, harvest date and references. Condition 2 crabs have recently gone through moulting while condition 3-4 crabs are in a more developed exoskeleton. All samples were stored in a freezer. The frozen samples were thawed for around half-day to unfreeze at moderate temperature before the measurements. Crab #1 was measured separately in an initial step in order to optimize the different experimental setups.

Table 1 : Snow crabs characteristics

| Crab | Shell wide (mm) | Claw height (mm) | Condition | Sampling date | Station | Observation |
|------|-----------------|------------------|-----------|---------------|---------|-------------|
| 1 | 103.84 | 19.88 | 2 | 26/08/2017 | GP066F | Immature |
| 2 | 107.92 | 21.91 | 3M/Skip | 26/08/2017 | GP066F | |
| 3 | 105.87 | 26.1 | 4 | 26/08/2017 | GP063A1 | |
| 4 | 102.83 | 19.83 | 2 | 26/08/2017 | GP050A1 | Immature |
| 5 | 106.96 | 26.95 | 3 | 26/08/2017 | GP093A1 | |
| 6 | 103.61 | 26.04 | 2 | 26/08/2017 | GP070F | |

4. LIBS Measurements

The measurement principle is described in Figure 1. A short laser pulse is focused onto a sample's surface. The material quickly heats up and vaporizes to form plasma. As the plasma cools down, the excited electrons return to their atom's ground states and emit photons. The atoms' emission is collected and is spectrally dispersed. Emission lines can then be analyzed to determine the elemental fingerprint of the vaporized material.

4.1 Experimental

The measurement was carried out using a Q-switched Nd:YAG laser that can deliver up to 300 mJ per pulse at a wavelength of 1064 nm. The pulse duration was about 9 ns FWHM and the optimal repetition rate was 2 Hz. The laser energy was adjusted to about 35 mJ. In these conditions, the estimated spot diameter onto the surface of the samples was about 600 μm . The focused spot created plasma. Therefore, the light emitted passed through the centre of a dichroic mirror positioned next to the plasma expansion direction and was then focused onto the entrance of an optical fibre bundle by an achromatic lens. The optical fibre bundle composed of 14 individual fibres of 100- μm core diameter collected and separated the light power in two

smaller fibre bundles composed of seven fibres each. The two small bundles were connected to the two entrances of a dual channel spectrometer (Avantes, Netherlands) which allowed analysis of all the emission lines located in the spectral range between 230 nm and 920 nm. The channel 1 was a 75 mm Czerny-Turner type UV/VIS spectrometer covering a spectral range of approx. 230 nm to 458 nm using a linear CCD detector with 2048 elements. The chosen configuration led to a linear dispersion of 19 nm/mm (i.e. 270 pm per pixel of 14 μm width). The channel 2 was a VIS/NIR covering a spectral range of 460 to 920 nm (VIS/NIR). Emission lines were identified by comparing the line wavelengths with the NIST atomic database [1].

The experimental setup for snow crabs samples used computer-controlled translation stages with three movable axes to support the sample holder. Moreover, the experimental setup and spectral data were controlled using a custom application developed in LabVIEW 2015 (National Instruments, Austin, TX, USA). In addition, spectral data post-processing with chemometrics was performed using SIMCA+ (Umetrics).

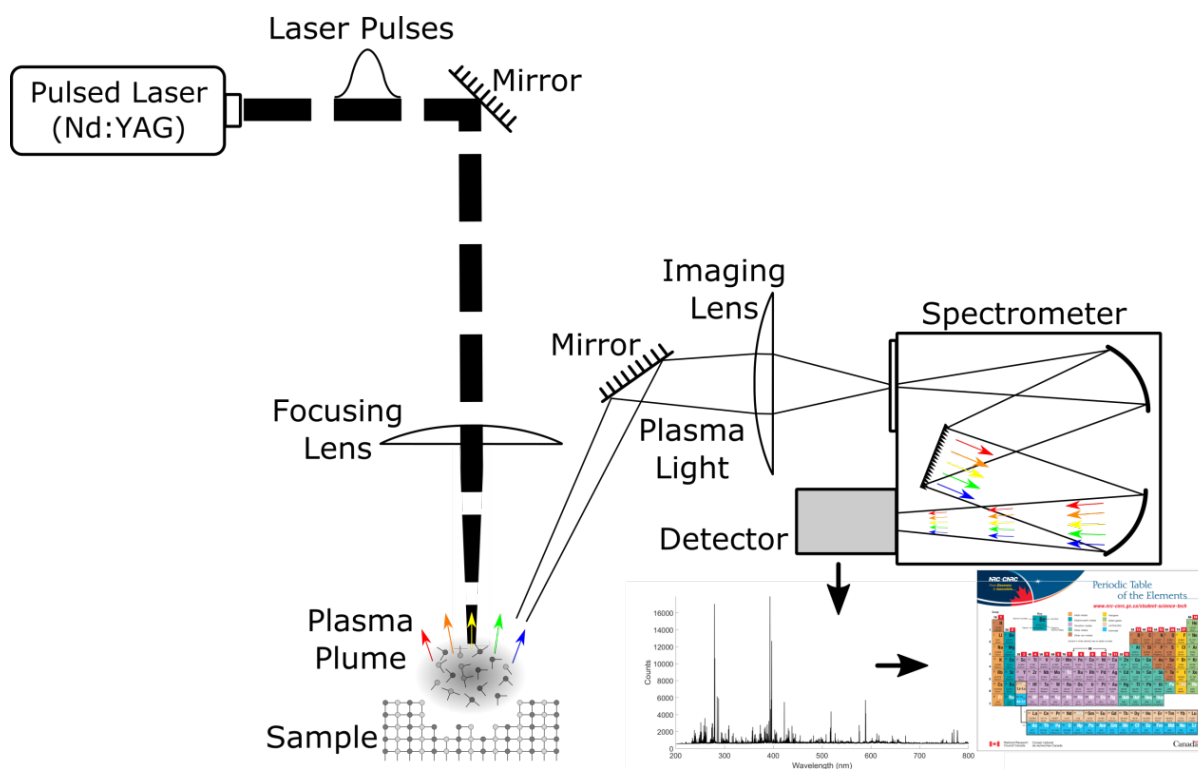


Figure 1 : LIBS experimental setup

4.2 Measurements

To achieve acceptable levels of representativeness of the measured material and accuracy of the acquired data, 2000 laser shots were used to perform a 2 x 2 mm² crater and to acquire

2000 spectra. Three replicates were carried on each snow crab part (cheliped, merus and intestinal region of the carapace) to evaluate the repeatability.

4.3 Results

Different snow crabs parts were analyzed by LIBS. Appreciable spectral differences were observed between the spectra acquired at the surface by the first 200 laser shots and the spectra acquired by subsequent laser shots. As an example, Figure 2 shows Si was only detected in the first 200 spectra acquired in the carapace. Its presence is probably due to the contamination of marine sand, so the first 200 laser shots (In the case of crab #4, 200 pulses were performed to ablate approximately 80 μm) were used to clean the surface and not taken into account for the analysis.

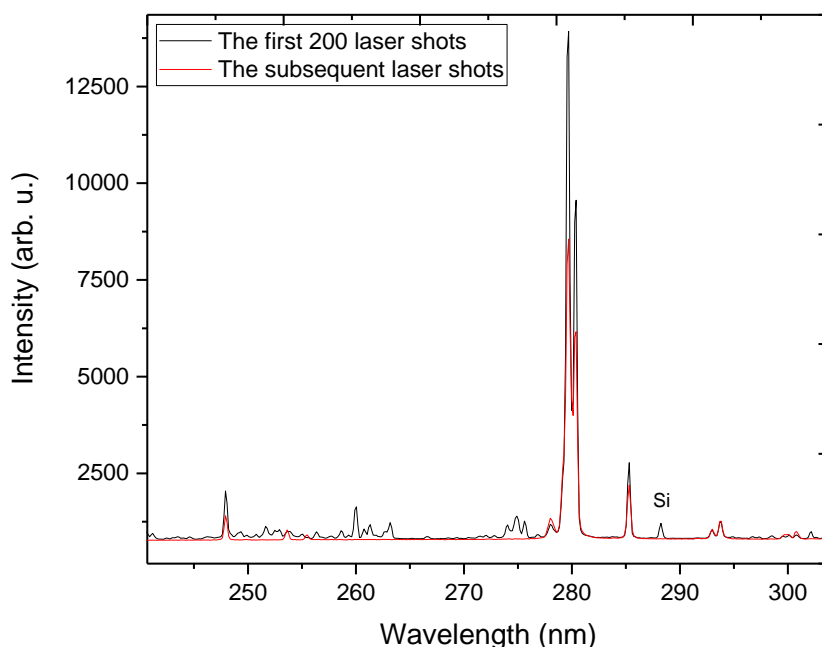
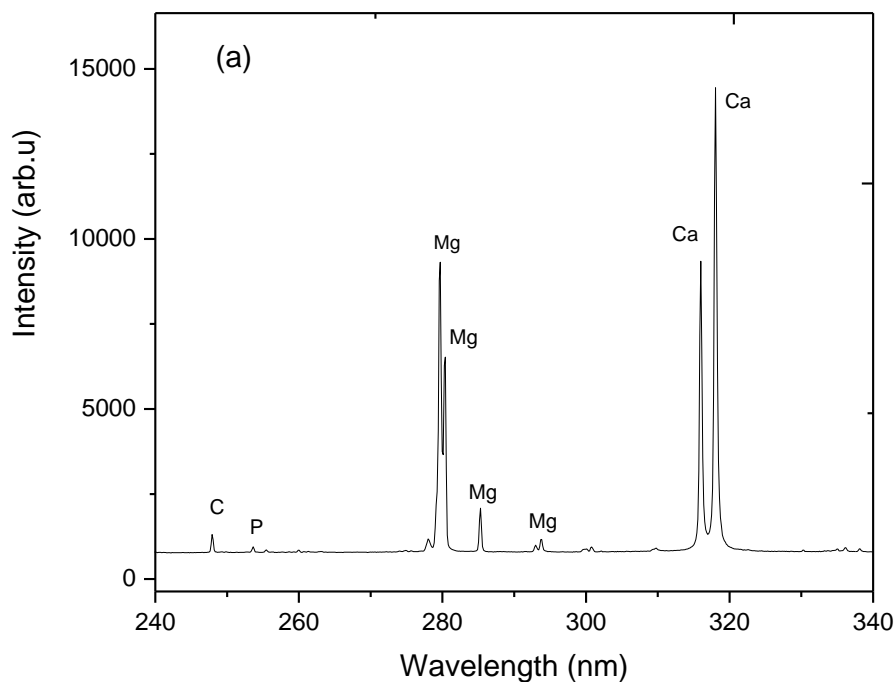


Figure 2 : LIBS spectra of dorsal carapace (Si from marine sand is shown in the spectra acquired by the first 200 laser shots).

The averaged representative spectra for the studied material are presented in Figure 3. As expected, the emission lines of Ca, Mg, K, H, Na and O were observed in all material. In addition, C and P lines were also detected as well as molecular bands corresponding to CaO. LIBS emission lines of different parts are summarized in Table 2.

Table 2 : Main emission lines detected by LIBS in snow crabs

| Element | Wavelength (nm) ¹ | | | | | | | |
|---------|------------------------------|------------|-------------|------------|------------|-----------|-----------|----------|
| C | 247.64(I) | | | | | | | |
| Ca | 315.88 (II) | 373.69(II) | 393.245(II) | 396.68(II) | 422.56(I) | 610.25(I) | 616.31(I) | 634.9(I) |
| CaO | 558.87 | 612.93 | 616.81 | | | | | |
| O | 777.19(I) | 777.41(I) | 844.63(I) | | | | | |
| K | 766.36(I) | 769.74(I) | | | | | | |
| Mg | 279.55(II) | 280.11(II) | 285.27(I) | 293.84 (I) | 383.829(I) | 518.36(I) | | |
| Na | 588.95(I) | 589.51(I) | | | | | | |
| H | 656.28 | | | | | | | |
| P | 253.5(I) | | | | | | | |



¹ Wavelengths are followed by (I) or (II) refer to emission from neutral atoms or emission from singly charged ions, respectively.

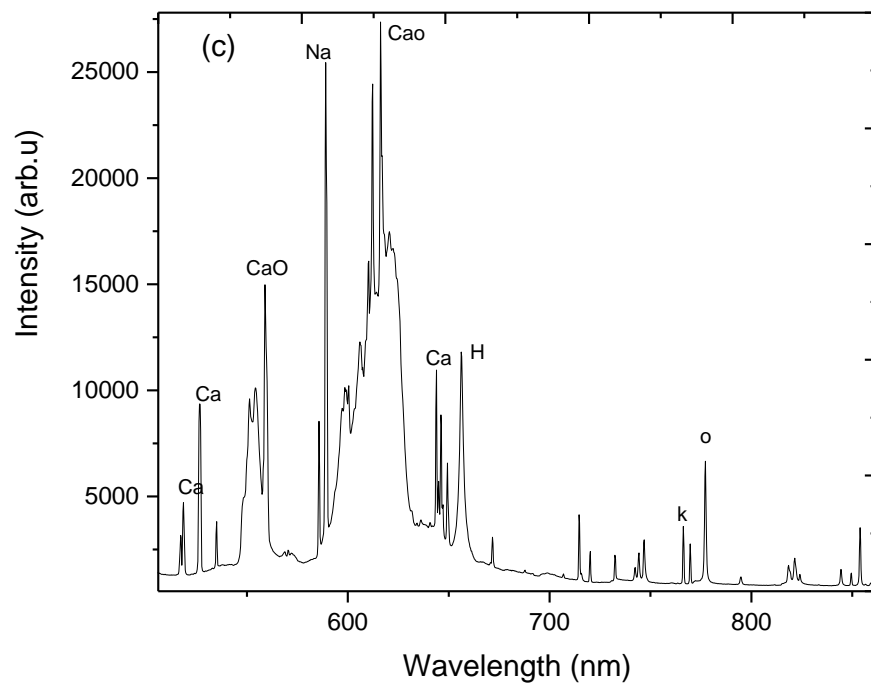
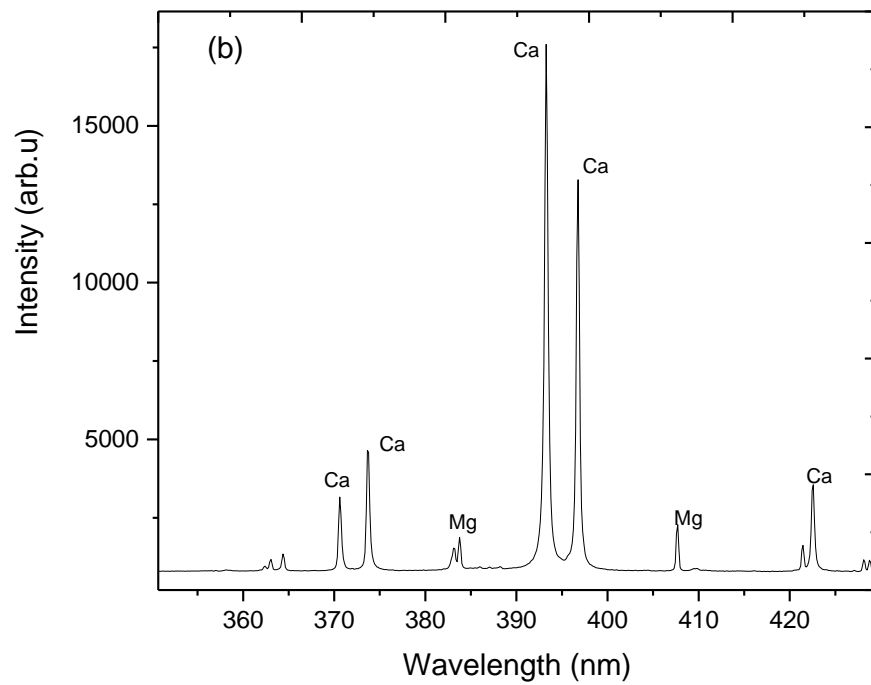


Figure 3 : LIBS spectra in different spectral ranges (a) 250–250 nm, (b) 350–430 nm and (c) 500–850 nm.

In the following, each part of the crab is studied separately to evaluate the feasibility of LIBS to discriminate the different moulting stages. In order to emphasize the differences observed, two approaches are used.

The first approach uses a univariate method where LIBS intensity ratios are used to classify different moulting stages. For this approach, LIBS depth profiling was done on each snow crab part. Emission spectra were averaged for every 200 laser shots. Each value was obtained by averaging values given by three replicates measured in three different locations. The error bars represent the standard deviation between the three replicates.

The second approach is a multivariate method called Principal Component Analysis (PCA) where the whole spectra are used to highlight variation between the different moults. PCA was carried out on 15 averaged spectra ie. five samples and three replicates of each snow crab part.

4.3.1 Univariate approach

As Ca and Mg are the major elements of the snow crabs, a study of the following intensity ratios is of interest: $\text{Mg(II)}/\text{Mg(I)}$ ratio and Mg/Ca ratio.

The ionic to neutral intensity ratio of Mg $\text{Mg(II)}/\text{Mg(I)}$ has already been used as an indicator of hardness of different matrices, namely enamel of human teeth, shells and eggs shell [2, 3]. The authors mentioned that, for a soft sample, the speed of the shock wave would be slowed down in comparison to the case of a hard target, due to the lack of a repulsive force on the irradiated surface, resulting in a reduction of the ionization effectiveness and then of the ionic to neutral intensity ratio. For this study, the ratio $\text{Mg(II)}/\text{Mg(I)}$ between the ionic magnesium line at 279.55 nm and the neutral line at 285.27 nm is calculated for each spectrum.

Mg/Ca ratio has already been used in anthropology and paleontology to distinguish tooth dental tissue and between the teeth of the groups and individuals [4]. It has been also used as an environmental proxy to reconstruct paleotemperatures and seasons of capture of molluscs [5, 6]. For the following, the ratio Mg/Ca between the magnesium line at 279.55 nm and the calcium line at 315.88 nm is calculated for each spectrum. Note that this ratio is not necessary equal to the absolute ratio of magnesium to calcium content. It depends on the intensity of selected lines of each element.

4.3.1.1 Cheliped of the Chela

Figure 4 shows the depth profiling of the $\text{Mg(II)}/\text{Mg(I)}$ ratio across the depth of the carapace for all crab samples. As shown, there is no significant difference between all the measured values.

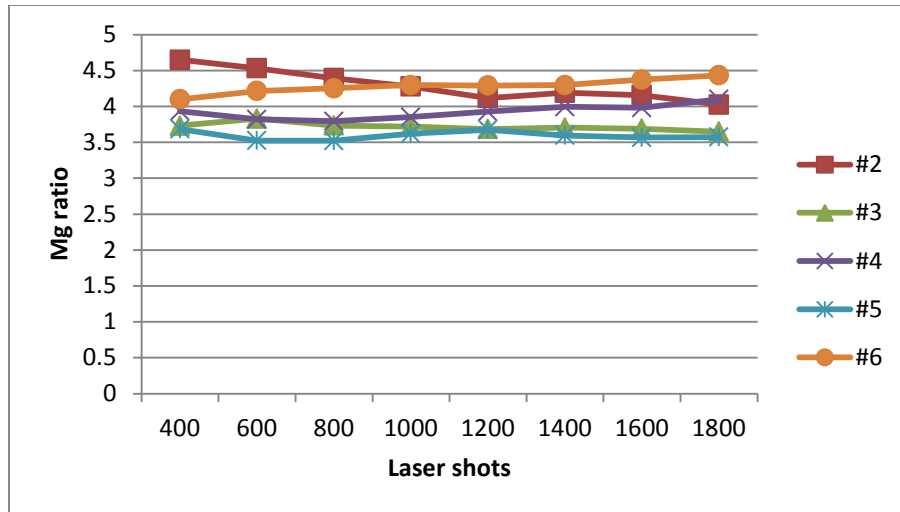


Figure 4 : Depth profiling of Mg(II)/Mg(I) ratios in chelipeds of different snow crabs

In contrast, Figure 5 shows that the Mg/Ca ratio behaviour is different. 2 groups are observed: a cluster grouping crabs #2 (condition 3M), #3 (condition 4) and #5 (condition 3) and a cluster grouping #4 (condition 2) and #6 (condition 2).

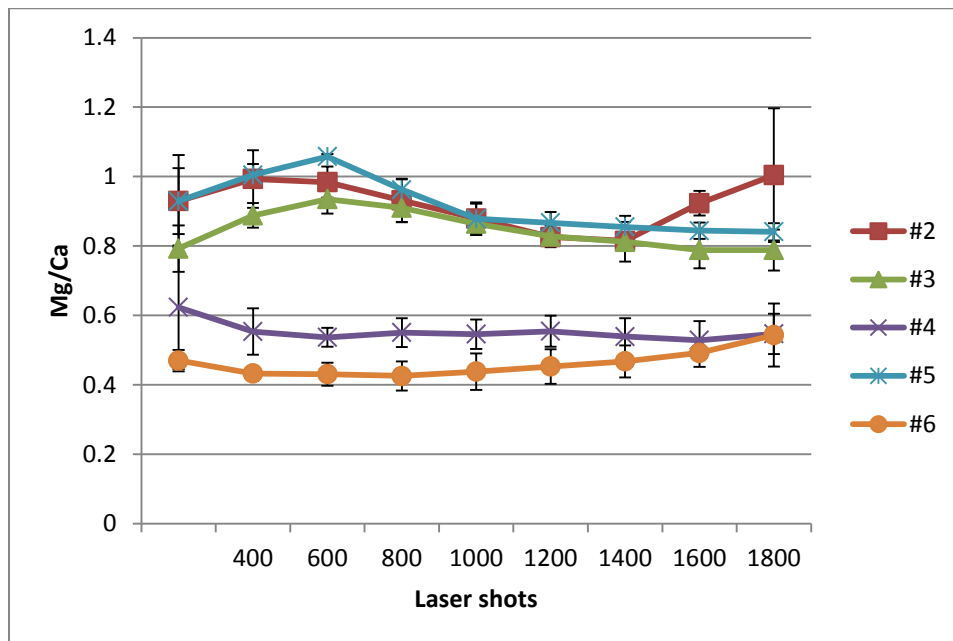


Figure 5 : Depth profiling of Mg/Ca ratios in chelipeds of different snow crabs

The Mg/Ca ratio values given in Figure 5 are averaged and displayed in Figure 6. Crabs #2, #3 and #5 have Mg/Ca ratios above 0.3, however, crabs #4 and #6 have Mg/Ca ratios are lower than 0.6. This result shows the ability of LIBS applied to cheliped to distinguish postmoulters (#2, #3, and #5) and “intermoulters (#4 and #6).

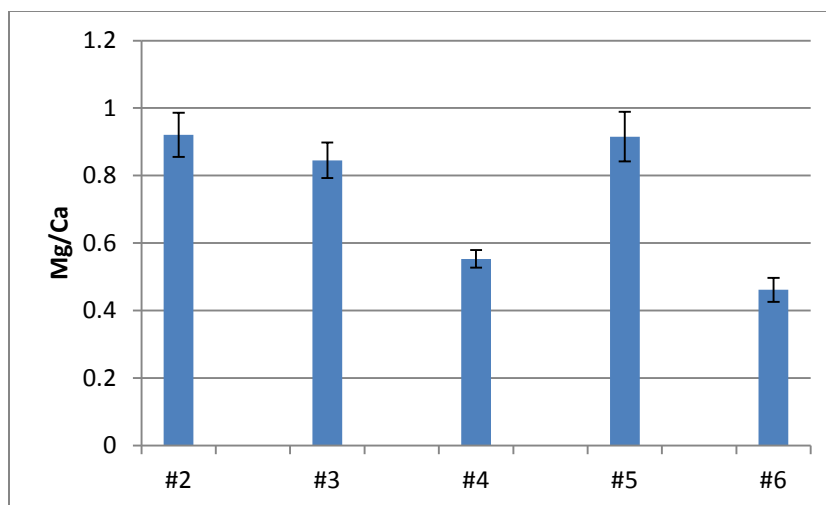


Figure 6 : Averaged Mg/Ca ratios in chelipeds for different snow crabs

4.3.1.2 Intestinal region of the carapace

Intestinal regions of the carapace of the five crabs were analyzed by LIBS and Mg(II)/Mg(I) ratios were determined. Figure 7 shows that this ratio decreases when laser shots increase for crabs #4 and #6. This behaviour is explained by the softness of the material. In fact, using the same number of laser shots, craters ablated in carapace of crab #4 (Figure 8) and #6 are deeper than those ablated in other crabs. This means that the carapace dorsal of crab #4 and #6 is probably less hard over the depth. Moreover the ratio of crab #4 decreases more quickly than the ratio calculated from crab #6. This can probably be explained by maturity degree of the crab at moulting condition 2, so immature crab has probably a softer carapace.

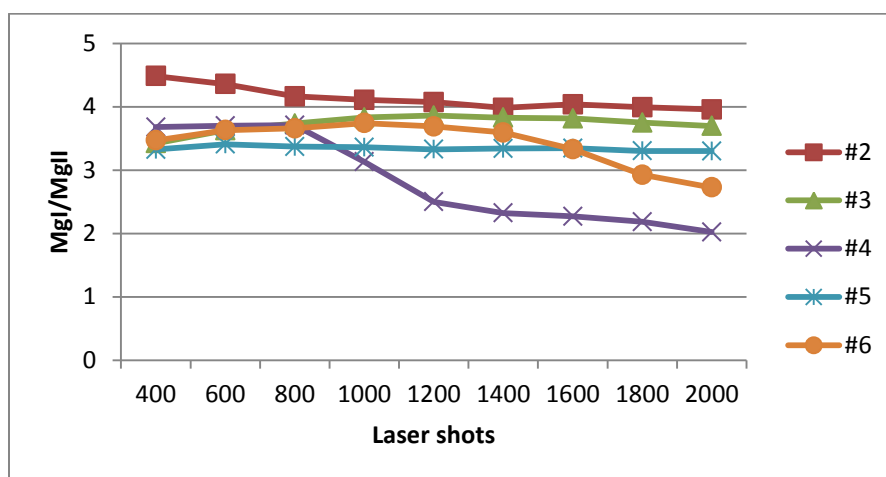


Figure 7 : Depth profiling of Mg(II)/Mg(I) ratios in carapace dorsal of different snow crabs

The averaged Mg/Ca ratio values measured in different carapaces are summarized in Figure 9. Crabs #3 and #5 (condition 4 and condition 3, respectively) exhibit a high Mg/Ca ratio compared to other crabs. Unlike for the cheliped results, crab #2 (condition 3M) exhibited a Mg/Ca value similar to values given by crab #4 and #6 (condition 2).



Figure 8 : Laser ablation marks on crab #4 (left) and crab #5 (right)

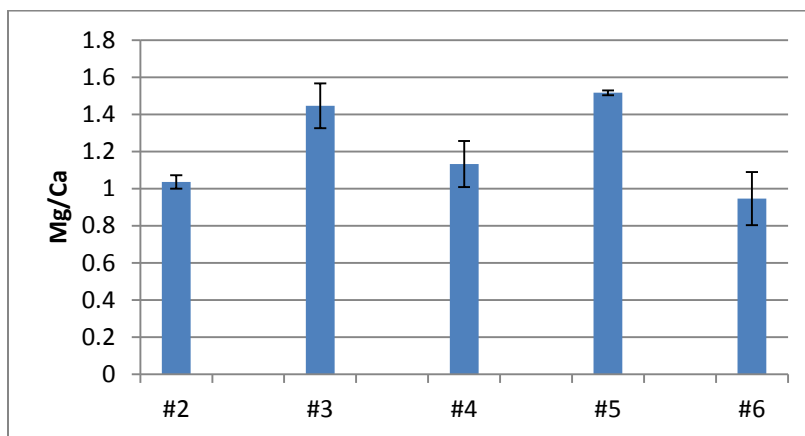


Figure 9 : Averaged Mg/Ca ratios in carapaces for different snow crabs

As a preliminary conclusion, the application of LIBS in the carapace can be useful to give an indication about the hardness of the material by investigating the depth profile of the Mg(I)/Mg(II) ratio, however, the Mg/Ca ratio is not useful to distinguish “postmoulters” and “intermoulters”

4.3.1.3 Merus of the 2nd pereopod

LIBS measurements were done in merus of different snow crabs. As the material is very thin and soft, only 800 laser shots including 200 shots for cleaning are sufficient to ablate the merus material (Figure 10). Using more laser shots creates a deeper crater that confines the plasma and therefore attenuates the LIBS signal which is useless for data analysis.



Figure 10 : Ablation mark on merus of crab #2

Mg(II)/Mg(I) ratio values are plotted as a function of the laser shot number in Figure 11. We see clearly two clusters: a group having high ratio values including snow crabs #3, #2 and #5, and a second group, having a ratio around 1.2, including snow crabs #4 and #6.

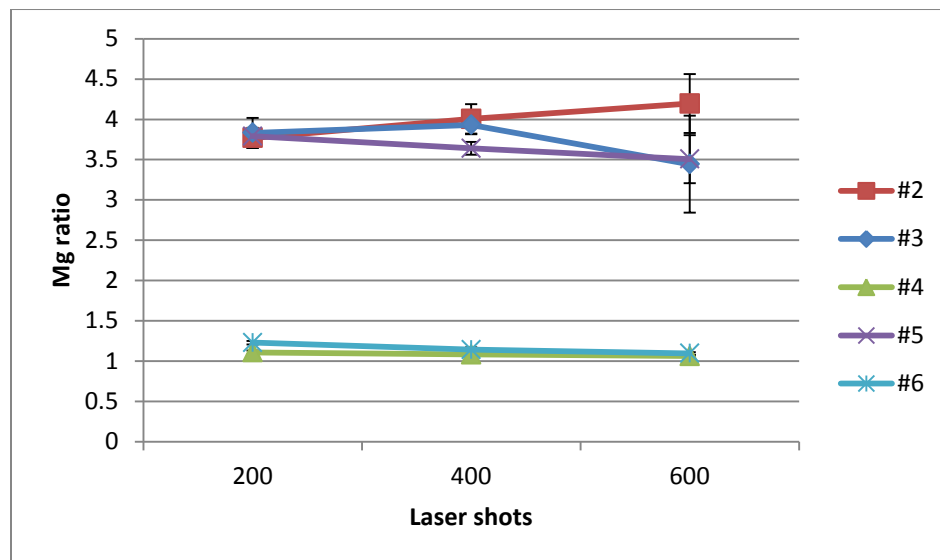


Figure 11 : Depth profiling of Mg(II)/Mg(I) ratios in merus of different snow crabs

Figure 12 shows the averaged values of Mg(II)/Mg(I) ratios. Crabs #2, #3 and #5 have ratios values around three times greater than ratios given by crabs #4 and #6. Based on the correlation between the extent of ionization of Mg(II) caused by the laser induced shock wave (SW) and the hardness of the target [2], this difference in ratio values means that merus of crabs #2, #3 and #5 are harder than merus of crabs #4 and #6. This procedure shows the ability of LIBS applied to merus to distinguish “postmoulters” (#2, #3, and #5) and “intermoulters” (#4 and #6).

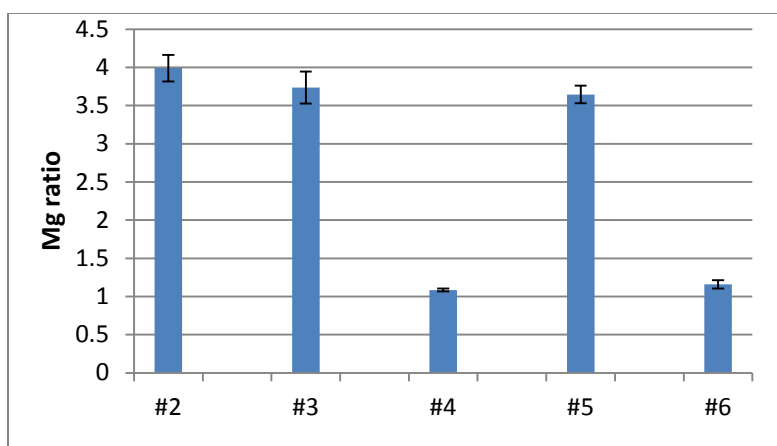


Figure 12 : Averaged Mg(II)/Mg(I) ratios in merus for different snow crabs

Regarding the Mg/Ca ratio, Figure 13 shows the same pattern as the carapace results. Crab #2 (condition 3M) has similar Mg/Ca ratio as crab #4 and #6 (condition 2). So far, there is no clear explanation of this behaviour.

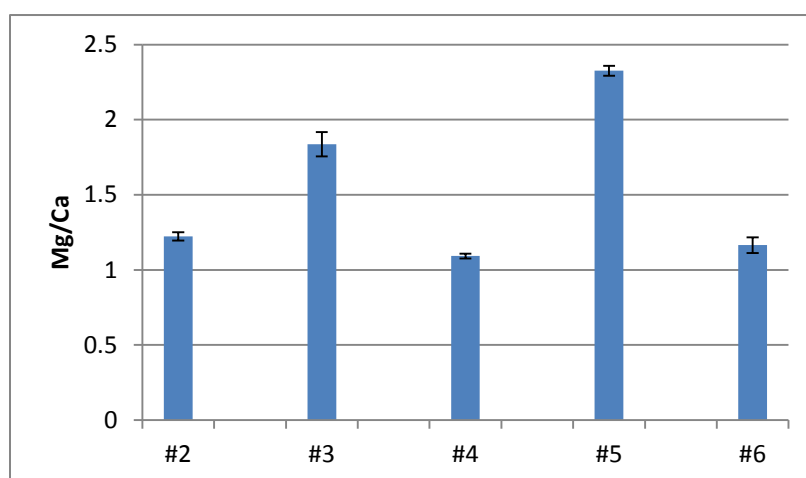


Figure 13 : Averaged Mg/Ca ratios in merus for different snow crabs

If we compare Mg/Ca ratio values of different snow crab parts, values given by chelipeds (<1) of all crabs are lower than the values of carapaces (between 0.8 and 1.6) and merus (between 1 and 2.5). It means that the cheliped is more calcified and mineralized than the other snow crab parts. This can be explained by the fact that the cheliped is the movable part of the cutting device and must be very hard compared to other parts.

On the other hand, although Mg(II)/Mg(I) ratios of the merus can be used to discriminate to identify “postmoulters”, this ratio in other snow crab parts cannot be used as an indicator of moulting. With the objective to study more dissimilarity between different moulting stages, more advanced chemometric approach such as PCA deserves to be evaluated.

4.3.2 Multivariate Analysis

LIBS data was analyzed through chemometric method to highlight variation throughout the snow crabs. More specifically, PCA [7] method was used to interpret the spectra as well as how snow crabs can be classified based on their spectral fingerprint. PCA is a well-known effective tool to visualize and to separate spectral data. For a given spectra dataset, a PCA analysis groups correlated variables to form “loadings”. For LIBS, these variables are the emission lines that are correlated. Typically, out of these groups of correlated variables, only the first ones are influents. Then, values called “scores” are attributed to each spectrum describing how well it fits with each of these extracted groups. PCA analysis presented in this section was performed using the averaged spectra of the 800 measurements for each location with three analyzed locations for each snow crab. LIBS spectra were normalized to reduce the signal intensity fluctuations by using standard normal variate (SNV) method [8]. Throughout this section, sample names are referred as the following XYZ with A is the crab part (C=Cheliped, D=Dorsal carapace and M=Merus), X is the crab number and YZ is the replicate number. For example, C301 refers to the cheliped of the crab #3 and the replicate 1. The moulting conditions are labelled in the legend.

4.3.2.1 Cheliped of the Chela

Figure 14 shows a PCA plot over 15 data points. The first component represents 68.8% of the variance whereas the second represent 18.5%. The high values of scores on the first principal component correspond to “postmoulters” crabs #4 and #6. In the reverse, the negative values of scores on the first component correspond to “intermoulters” #2, #3 and #5 and 8. We see clearly that crab spectra are sorted by condition moulting from condition 4 to condition 2. The separation is clearer for condition 2 and other conditions, while the distinction between condition 3 and condition 4 is not sharply defined.

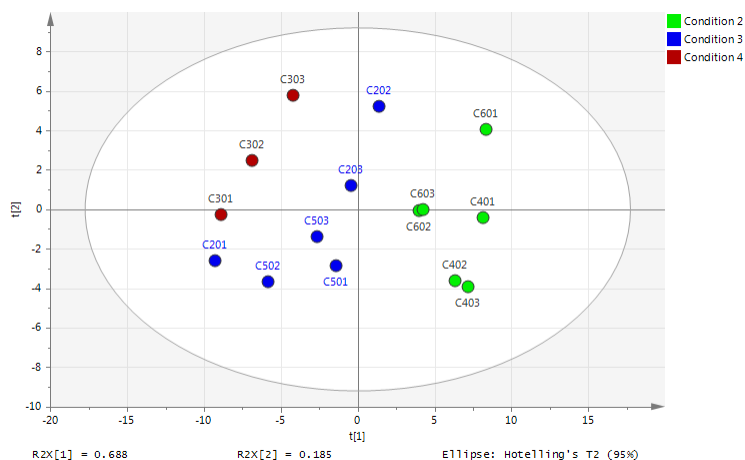


Figure 14 : PCA score plot of cheliped LIBS spectra. The legend includes the moulting condition.

In order to understand the spectral origin of each principal component, loadings are investigated. Figure 15 shows the first two principal component loadings plot. The positive loadings reflect the LIBS lines of calcium, however, the negative loadings are correlated with Na

and H. This indicates that cheliped of “postmoulters” are more calcified and composed of less hydrogen and sodium than “intermoulters”.

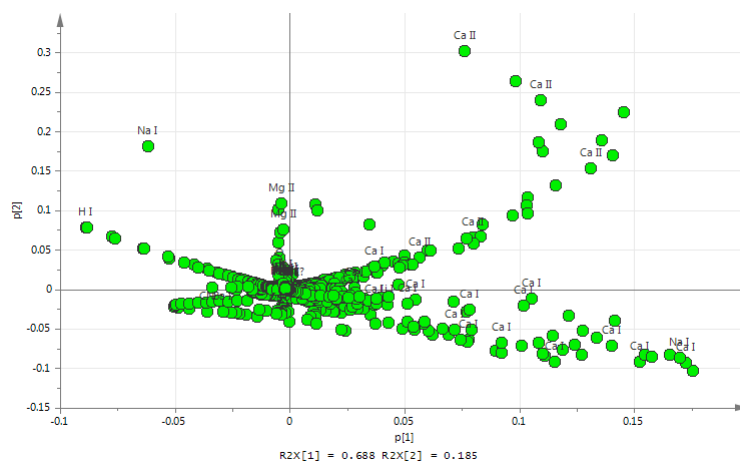


Figure 15 : PCA loadings plot of cheliped LIBS spectra.

4.3.2.2 Intestinal region of the carapace dorsal

Figure 16 shows a PCA plot of dorsal carapace spectra. The top right corner corresponds to crab #5 and #3, however, crab #2 who has moulting condition 3M is located in the reverse corner. In addition, the negative values of scores on the 2nd principal component correspond to “postmoulters” crabs #4 and #6 (condition 2). The loading (not shown here) doesn’t give a clear correlation and therefore explanation for this discrimination.

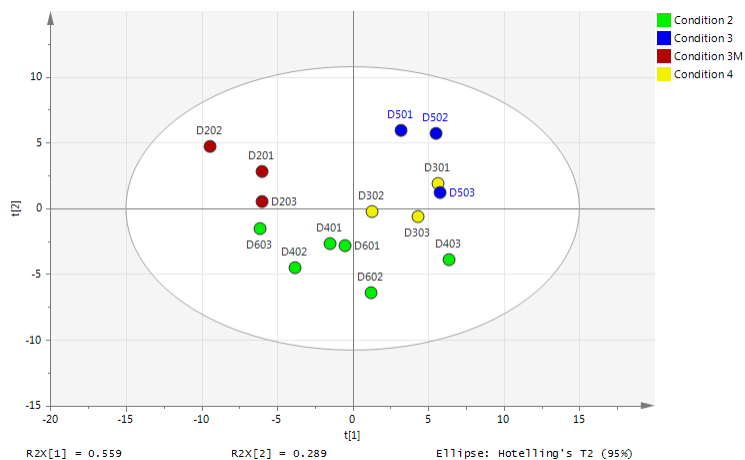


Figure 16 : PCA score plot of dorsal carapace LIBS spectra. The legend includes the moulting condition.

4.3.2.3 Merus of the 2nd pereopod

Figure 17 shows a PCA scores plot of merus spectra. The first component represents 96.4% of the variance whereas the second represent 2.4%. The positive values of scores on the first principal component correspond to “postmoulters” crabs #4 and #6. In the reverse, the negative values of scores on the first component correspond to “intermoulters” #2, #3 and #5 which contain more Ca (Figure 18). Conversely, snow crabs #4 and #6 contain more Na and H, which is in contrast with the cheliped behaviour over different moulting stages. This result is in accordance with the Mg(II)/Mg(I) ratio interpretation. It can be explained by hard material containing more calcium; however, a softer material contains more sodium and water.

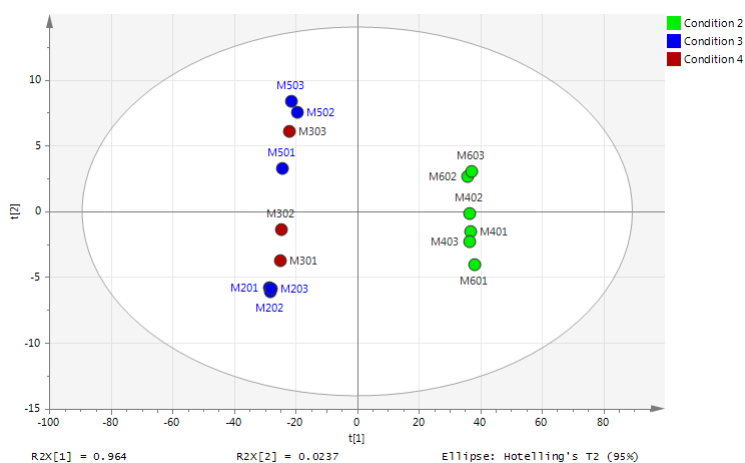


Figure 17 : PCA score plot of merus spectra. The legend includes the moulting condition.

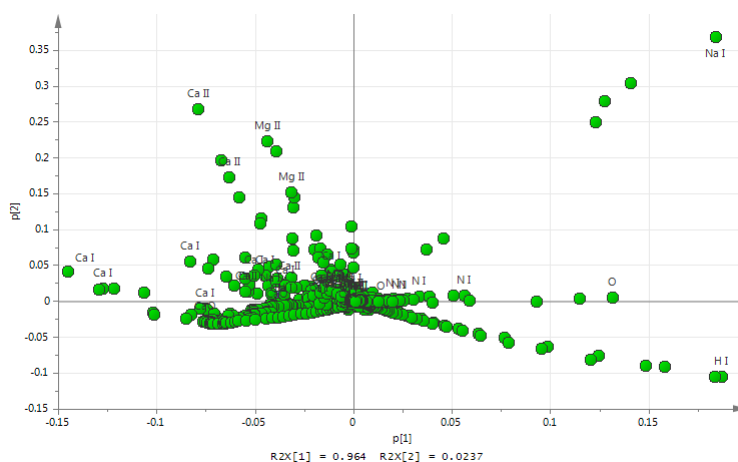


Figure 18 : PCA loading plot of merus spectra.

In conclusion, compared to other methods of analysis, advantages of LIBS include multi-elemental analysis, rapidity, portability and no sample preparation. The use of intensity ratios of line permits to discriminate and separate “intermoulters” and “postmoulters”. Regarding coupling LIBS to PCA, the approach shows that the analysis of the cheliped could give discrimination

between the 3 moulting conditions (2, 3 and 4). Although LIBS could offer an opportunity for the depth profiling, a prior knowledge of the thickness is needed as the ablation rate varies with the snow crab part and with the location of analysis.

5. OCT Measurements

Optical coherence tomography (OCT) is an interferometric optical technology that has been developed in the early nineties to provide cross-sectional imaging of biological tissues. The imaging contrast of OCT is provided by variations of refractive index causing reflections within a tissue. These variations in refractive index can occur at a rather large scale, like those between layers of tissues, or at a smaller-scale, like those related to cellular structures. OCT performs cross-sectional imaging over a few millimetres in a tissue, with a typical resolution of the order of 10 micrometers. Imaging depth in a tissue is limited by the absorption and scattering of light by the various tissue structures. OCT systems can be designed to provide an even better resolution of a few micrometers, often at the expense of the depth over which imaging can be performed.

Nowadays, OCT is divided in two different approaches: spectral-domain OCT (SD-OCT) and swept-source OCT (SS-OCT). Both approaches are based on the processing of an interferometric signal recorded as a function of the wavelength. The main difference between the two approaches is that the wavelength dependency is handled at the detection level with a spectrometer in SD-OCT, while it is handled at the illumination level with a swept-source laser in SS-OCT. Both approaches provide the same quality of cross-sectional imaging. SD-OCT has a measurement range of at most a few millimeters while SS-OCT has a measurement range that can reach hundreds of millimeters. The crab shell being an uneven surface, a large measurement range is preferable since it allows imaging over a larger area. All measurements in this report were obtained with an SS-OCT system.

5.1 Experimental

The main components of a SS-OCT system are depicted in Figure 19. Light from a swept-source laser is sent through an optical fiber to a fiber coupler which splits the light into the two arms of an interferometer: the sample arm and the reference arm. The sample arm contains optical elements that focus the light on the sample and collect the light reflected from the sample. The reference arm contains a mirror that reflects the light back into the fiber. Light from the sample arm and the reference arm are then sent back to the coupler where they interfere. The interference is recorded by a high-speed digitizer as the wavelength of the laser source is swept. The processing of the interference signal then provides a through-depth imaging measurement which is referred to as an A-Scan. The sample arm contains a transverse scanning mechanism that allows moving the measurement location across the surface. A cross-sectional imaging of the sample, called B-Scan, is obtained by combining adjacent A-Scans. In section 5.3, we present many cross-sectional images measured on crab shells.

All OCT measurements were performed with a proprietary system developed at NRC. Within that system, all components of Figure 19 contained in the blue box were integrated into an interferometer box. The swept-source laser swept over 80 nm around a wavelength of 1550 nm. The sample arm included an optical scanner which was connected to the interferometer box by an optical fiber and a few electrical wires. The fact that the sample arm can be located remotely from the main system is a great asset of an OCT system. The NRC OCT system was developed for another application and is quite unique in its genre. It was selected for the project since the

optical scanner allows measurements up to 100 mm in width which was ideal to image the whole shell surface. The optical scanner head along with the sample are presented in Figure 20. The scanner has a special shape since it was designed to fit in a very specific location with space constraints. The light was sent and collected through the dark slit located just above the crab in Figure 20. The OCT system was a high-speed system performing 140 000 A-Scans measurements per second and the measurement depth range was 14 mm.

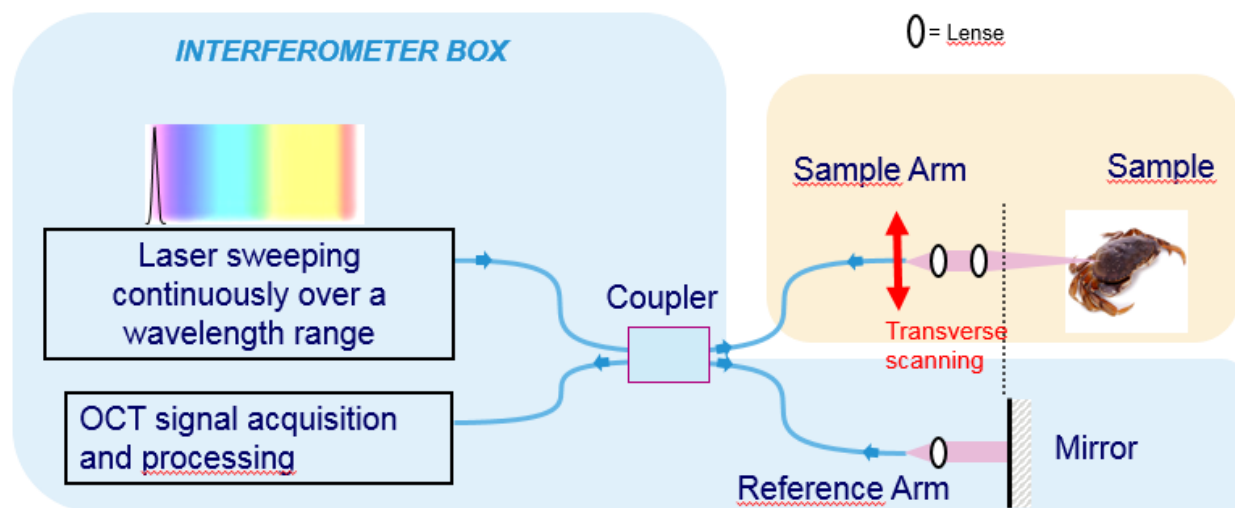


Figure 19 : Swept-source OCT system.

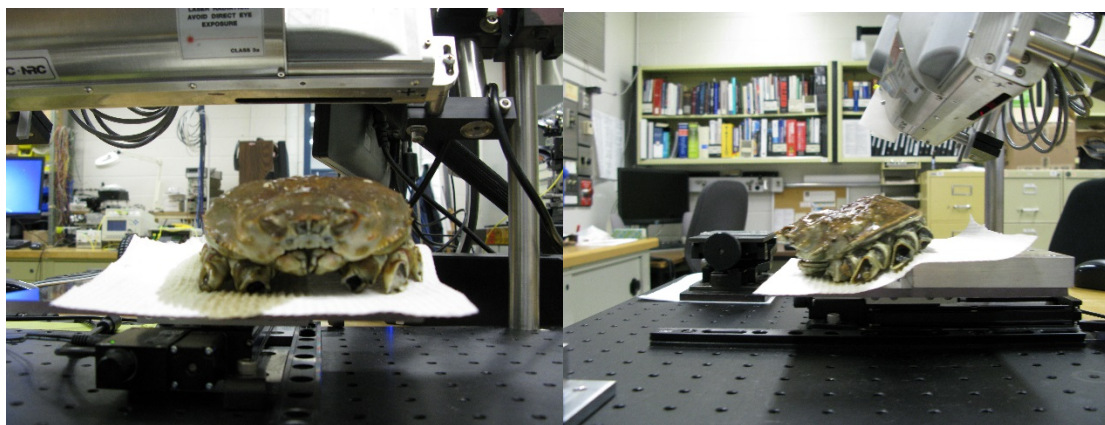


Figure 20 : Optical scanner and crab sample.

5.2 Measurements

Most measurements were carried out with the low resolution high speed OCT setup shown in Figure 20. It can typically scan objects in a 100 mm x 100 mm x 10~100 mm volume with a 100 μm x 100 μm x 30 μm resolution. The pixel size was chosen to be 60 μm x 60 μm x 14 μm to slightly oversample the volume under examination while exploiting the full potential of the system's resolution. It took about 5-15 s to scan a crab shell with this system. The largest scans, displayed in Figure 21 and Figure 22, took 30 s to acquire. Note that a resolution of 30

μm (depth) and $100\ \mu\text{m}$ (transverse) are a little larger than what is usually found in OCT systems. These choices were made to enable whole shell imaging. A different system was also used to acquire smaller images at a higher resolution. This other system typically scan objects in a $20\ \text{mm} \times 20\ \text{mm} \times 8\ \text{mm}$ volume with a $25\ \mu\text{m} \times 25\ \mu\text{m} \times 10\ \mu\text{m}$ resolution. The results obtained with that system are presented in section 5.3.4.

5.3 Results

Figure 21 and Figure 22 demonstrate that, with an adapted scanning method, a whole crab can be imaged. Although the images seem to be 3D surface images, the datasets are whole 3D point clouds. It is the opacity of the rendering that limits the view to the surface of the point clouds. Subsequent results will be more focused on images of the shell's interior to investigate their structures and thickness by providing also cross-sectional views. When photos of the crabs were available for the figures, the scanned area was delimited in blue.

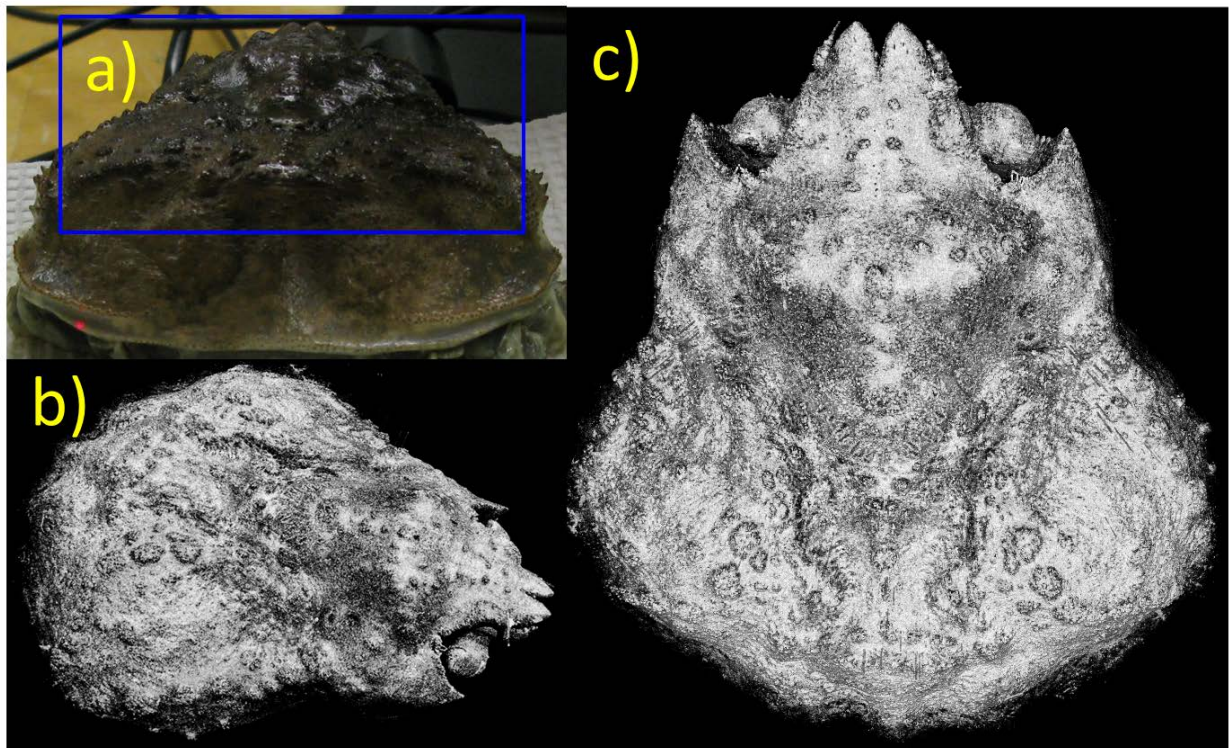


Figure 21 : (a) Top of crab #1 carapace. (b, c) OCT tomographic reconstructions.

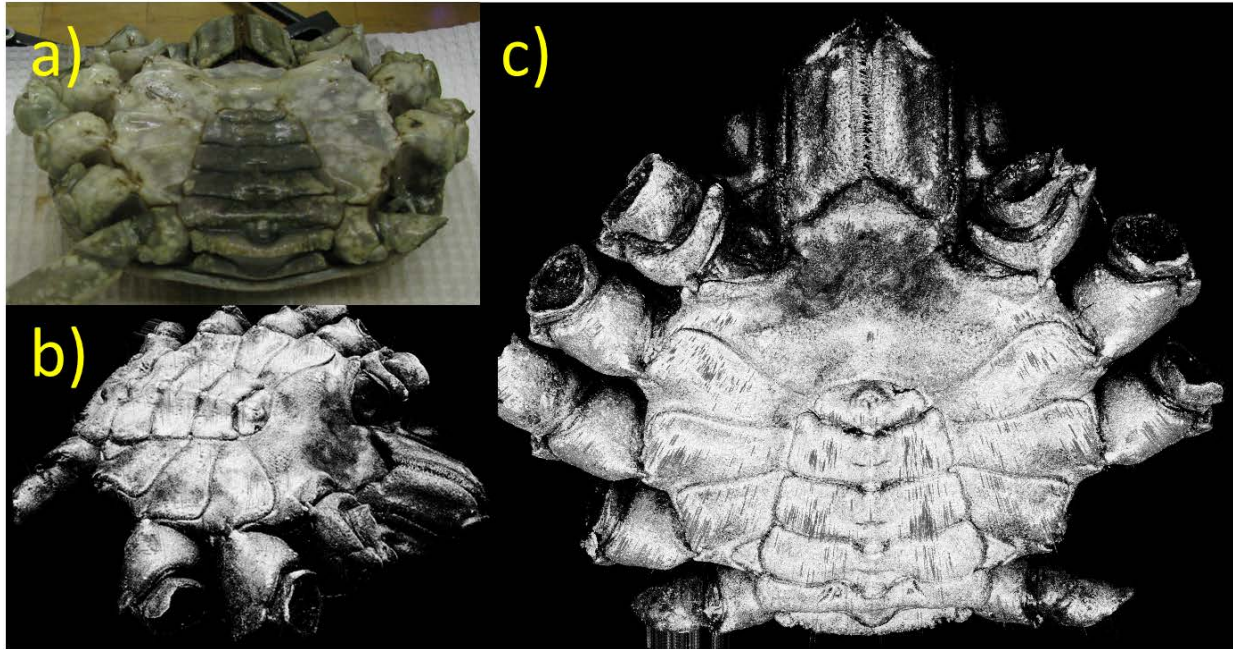


Figure 22 : (a) Bottom of crab #1 carapace. (b, c) OCT tomographic reconstructions.

The crab shell is composed of a stack of layers: the epicuticle ($\approx 10 \mu\text{m}$), the exocuticle, the endocuticle and the membranous layer. The next layer, beneath the shell, is the epithelium. Condition 2 crabs differ from condition 3, 3M and 4 crabs mostly by the thickness of their membranous layer and epithelium. We would expect to see slightly thinner shells without a membrane layer in condition 2 crabs compared to other conditions [9]

It must be kept in mind that OCT measures an optical thickness. To extract the real shell thickness, the measured values must be divided by its refractive index. The refractive index of a crab shell is most likely in a range between 1.33 (water) and 1.7 (a value slightly more than bones). Additionally, softer crab shells (postmoult) contain more water and should have a lower refractive index than hard shells. This must be kept in consideration for the interpretation of the results that follow. Since the refractive index is not exactly known for the tissue, dimensions in the images in this report are not scaled to take this effect into account. Note that OCT could be used to measure the refractive indices of the various shells, something that could be done in a follow-up project.

To fit in the report, many of the original images had to be downgraded in resolution. We encourage the reader to look at the original images, provided with the report, to fully appreciate the level of details in the crab shell structure. These images also include crab #2 (condition 3M/skip) and crab #6 (condition 2) which are not included in the report to avoid burdening it with too many repetitive images.

5.3.1 Cheliped of the Chela

The ventral side of the chela was imaged with the system. The tomographic reconstruction of this portion of the chela for crab #4, #5 and #3 are presented in Figure 23(a), Figure 24(a) and

Figure 25(a). The most relevant information for this study is found in the B-Scan images shown in Figure 23(c-d), Figure 24(b-c) and Figure 25(b-c). These images are sections of the volume taken in the green and red planes shown in each tomographic reconstruction. The color of the letter identifying each subfigure matches the plane it came from. A B-Scan section shows structural information of the inside of the tissue. Multiple layers can be seen in the crab shells. In most cases, by playing with the contrasts, it is even possible to see the soft tissue below the carapace.

The B-Scan images obtained in the different crabs are compared. In crab #4 (Figure 23), only two layers are clearly apparent, the first one returns a very bright signal and has an optical thickness ranging from 200 to 300 μm . It is most likely the epicuticle and exocuticle. Below that, a second layer with a similar optical thickness is observable, but it returns a much lower signal. This layer is most likely the endocuticle. The tissues were not in perfect condition since the crabs were dead. In some of them, the soft tissue detached from the shell and the gap got filled with air instead. This can add a narrow bright structure at the lower interface of the shell that should be harder to see in live crabs. This feature is much more apparent in Figure 31(b-c) where the contrasts allow seeing the soft tissue as well as the air gap between the shell and that tissue.

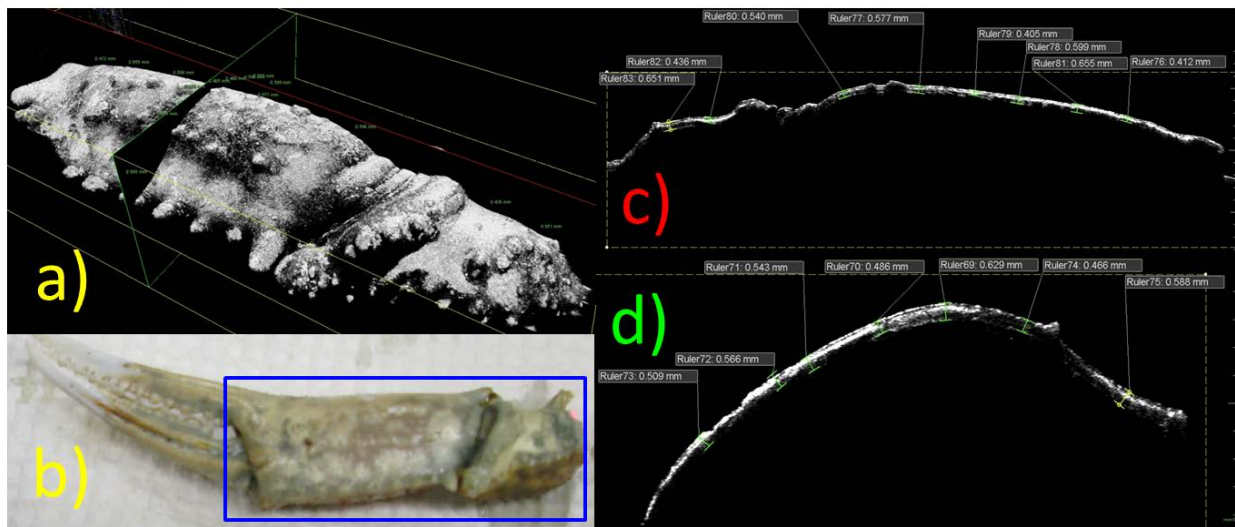


Figure 23 : (a) Tomographic reconstruction of (b) the cheliped of crab #4 (condition 2). (c, d) B-Scan reconstruction in the red and green planes of a) showing the shell thickness.

In crab #5 (Figure 24), a layer below the first two starts to become apparent. This new layer is most likely the membranous layer. The shell is thicker as well, with optical thickness ranging from 700 to 1000 μm .

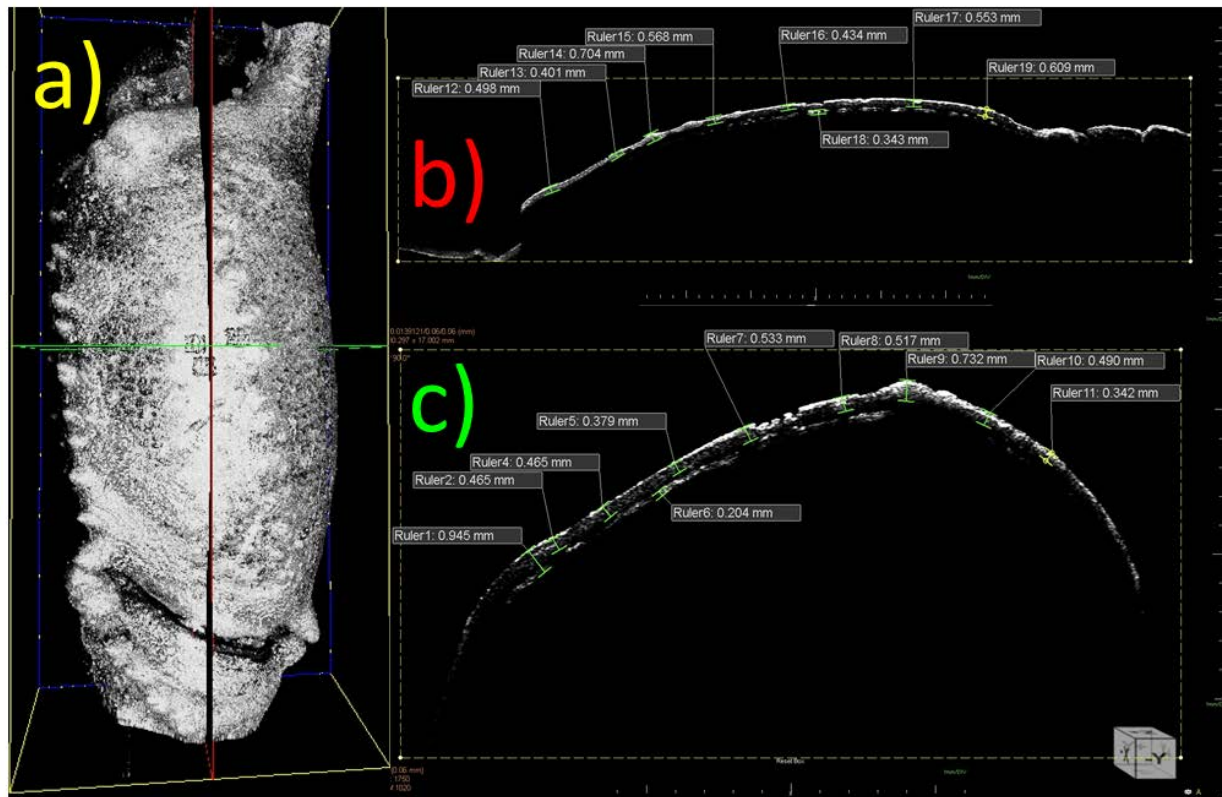


Figure 24 : (a) Tomographic reconstruction of the cheliped of crab #5 (condition 3). (b, c) B-Scan reconstruction in the red and green planes of a) showing the shell thickness.

In crab #3 (Figure 25), the layer below the first two is better defined and is thicker. The signal in the second layer appears to be smoother as well. Overall, it seems easier at this stage to identify in the OCT images the exocuticle, the endocuticle and the membranous layer stack forming the crab shell. The shell optical thickness is still ranging from 700 to 1000 μm . The three square structures visible near the intersection of the red and green planes are LIBS ablation scans that were performed prior to OCT measurement. The areas that were ablated are also visible in the B-Scan sections.

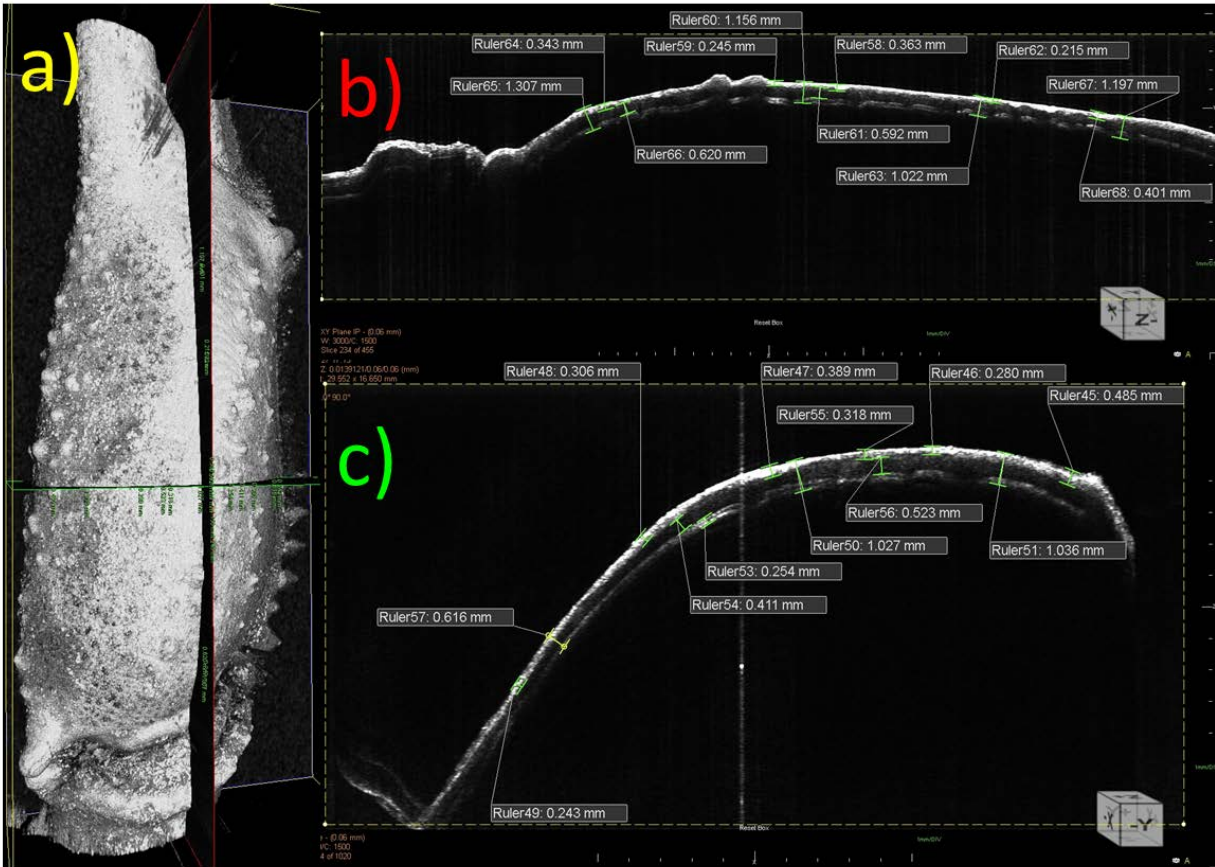


Figure 25 : (a) Tomographic reconstruction of the cheliped of crab #3 (condition 4).
(b, c) B-Scan reconstruction in the red and green planes of a) showing the shell thickness.

5.3.2 Intestinal region of the carapace

The dorsal intestinal region of the carapace was imaged with the system. The tomographic reconstruction of this portion of the carapace for crab #4, #5 and #3 are presented in Figure 26(a), Figure 27(a) and Figure 28(a). The most relevant information for this study is found in the B-Scan images shown in Figure 26(b-c), Figure 27(b-c) and Figure 28(b-c).

The B-Scan images obtained in the different crabs are compared. In crab #4 (Figure 26), the shell optical thickness is ranging from 700 to 900 μm . There seems to be a first layer returning a bright signal that should be the exocuticle followed by a second layer returning less light that is probably the endocuticle. A narrow bright structure at the lower interface of the shell is sometimes visible and might be caused by air pockets under the shell. There seems to be more signal in the shell at the back of the carapace, but that might just be caused by the orientation of the shell surface relatively to the scanning laser beam.

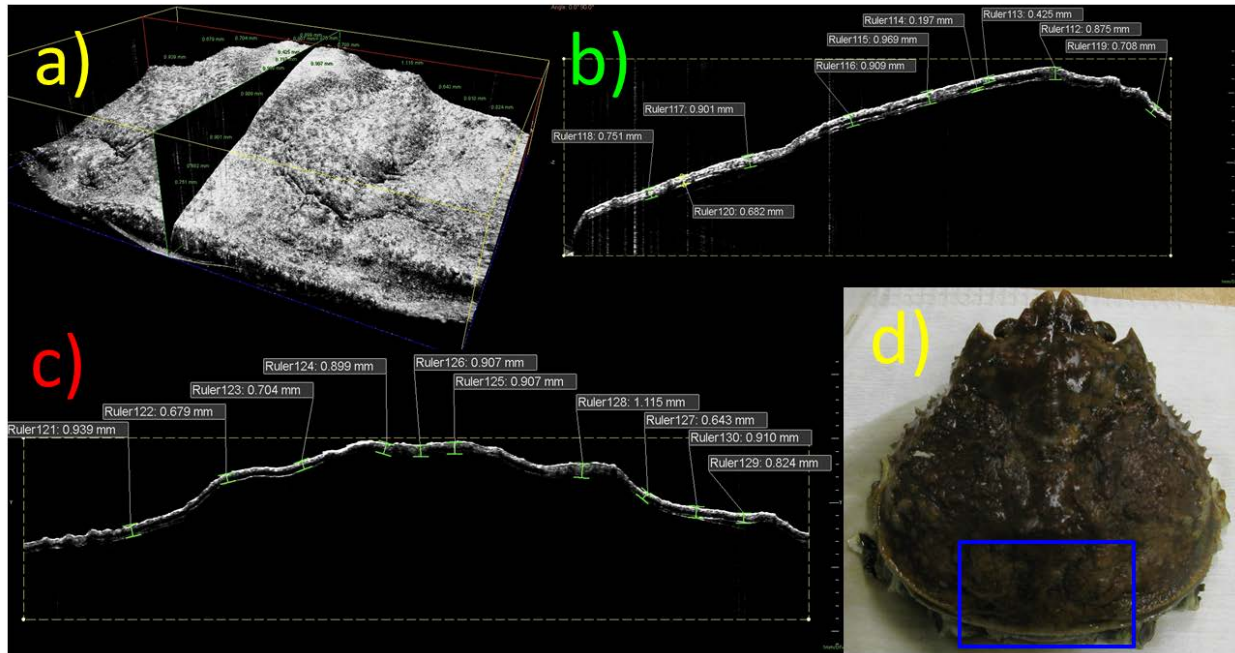


Figure 26 : (a) Tomographic reconstruction of (d) the carapace intestinal region of crab #4 (condition 2).
(b, c) B-Scan reconstruction in the green and red planes of a) showing the shell thickness.

In crab #5 (Figure 27), it is very clear that we are dealing with multiple layers. The first and the third one return a strong signal while the second one appears much darker. In some regions, other structures are also visible under that. The shell is slightly thicker as well, with optical thickness ranging from 800 to 1100 μm .

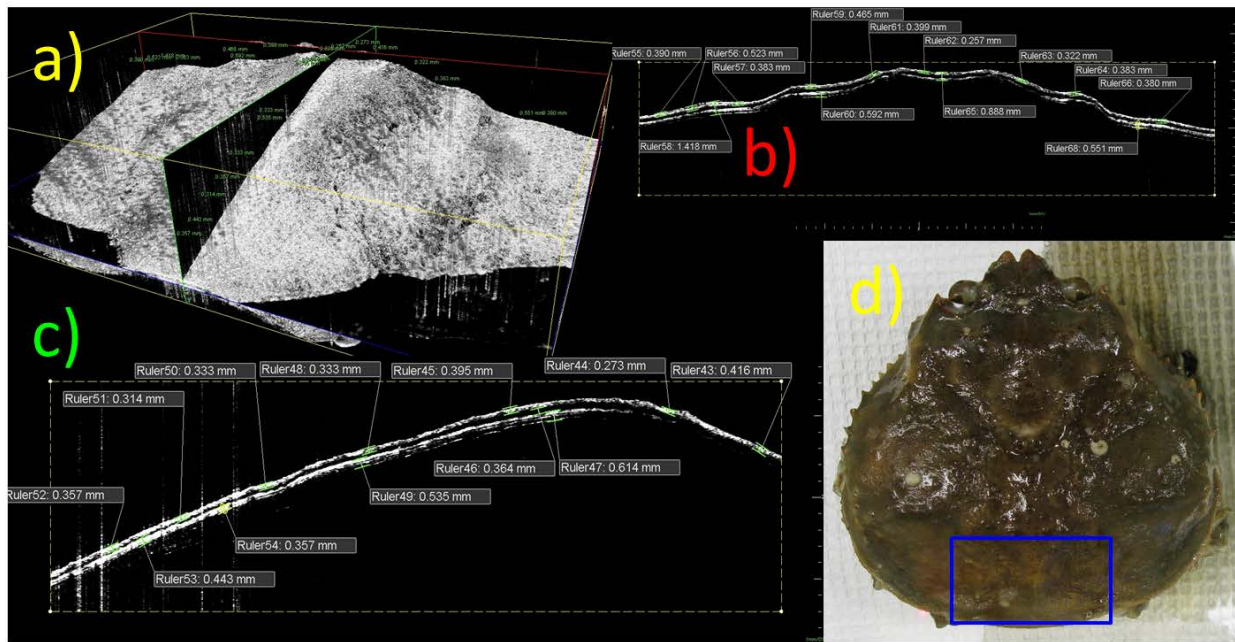


Figure 27 : (a) Tomographic reconstruction of (d) the carapace intestinal region of crab #5 (condition 3).
(b, c) B-Scan reconstruction in the green and red planes of a) showing the shell thickness.

In crab #3 (Figure 28), something very similar to crab #5 (Figure 27) is obtained, but the third layer is not as sharply defined as in crab #5. The shell optical thickness still seems to be ranging from 800 to 1100 μm .

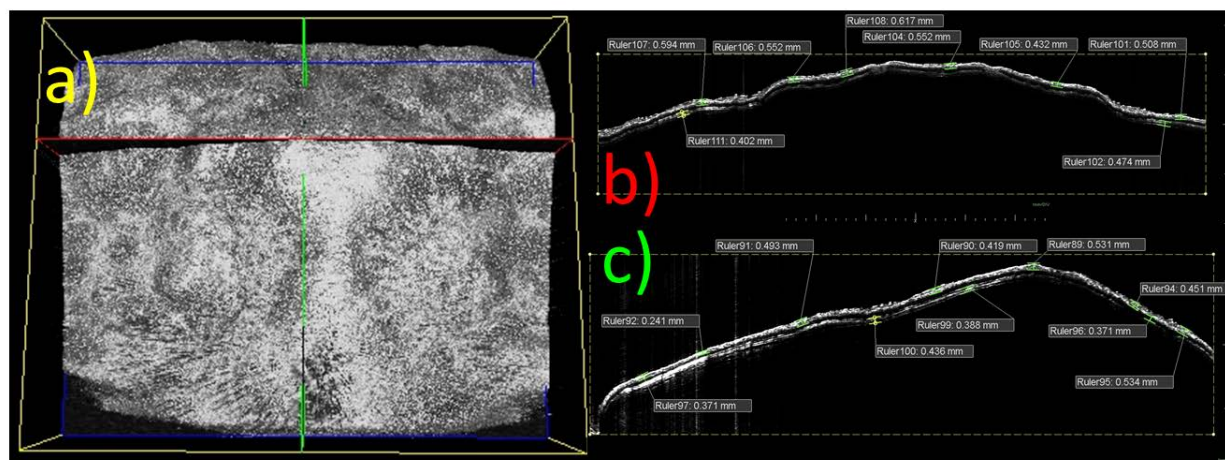


Figure 28 : (a) Tomographic reconstruction of the carapace intestinal region of crab #3 (condition 4). (b, c) B-Scan reconstruction in the green and red planes of a) showing the shell thickness.

5.3.3 Merus of the 2nd pereopod

The ventral side of the Merus of the 2nd pereopod was imaged with the system. The tomographic reconstruction of this portion of the chela for crab #4, #5 and #3 are presented in Figure 29(a), Figure 30(a) and Figure 31(a). The most relevant information for this study is found in the B-Scan images shown in Figure 29(c-d), Figure 30(b-c) and Figure 31(b-c).

In crab #4 (Figure 29), the shell optical thickness is ranging from 400 to 500 μm . The carapace on the Merus is thinner. A layer structure is observed, but it changes depending of the area in the image which makes it challenging to interpret. The four LIBS craters seen in the photo were not part of the green and red planes and the dark portion of the red plane is hiding them in Figure 29(a).

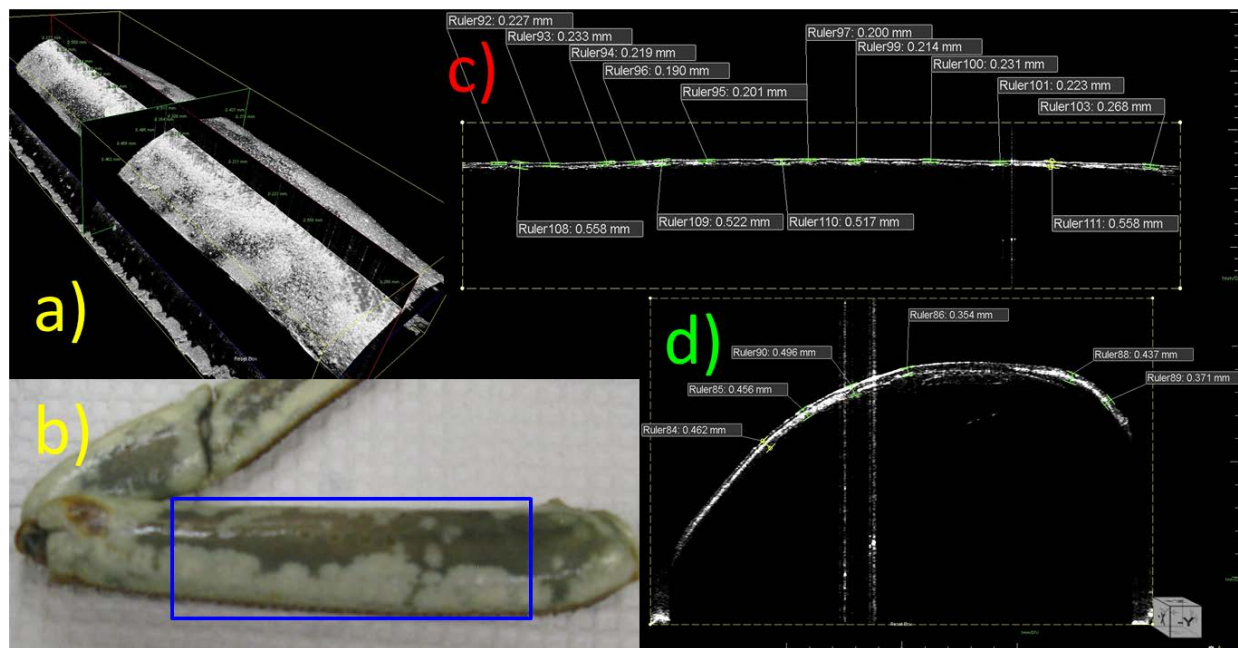


Figure 29 : (a) Tomographic reconstruction of (b) the merus of crab #4 (condition 2). (c, d) B-Scan reconstruction in the red and green planes of a) showing the shell thickness.

In crab #5 (Figure 30), multiple layers are present again. The shell is slightly thicker as well, with optical thickness ranging from 600 to 700 μm . The LIBS craters appear clearly in the OCT images and the crab soft tissue is visible in Figure 30 (b-c). Unfortunately, they appear very blurred in the photo.

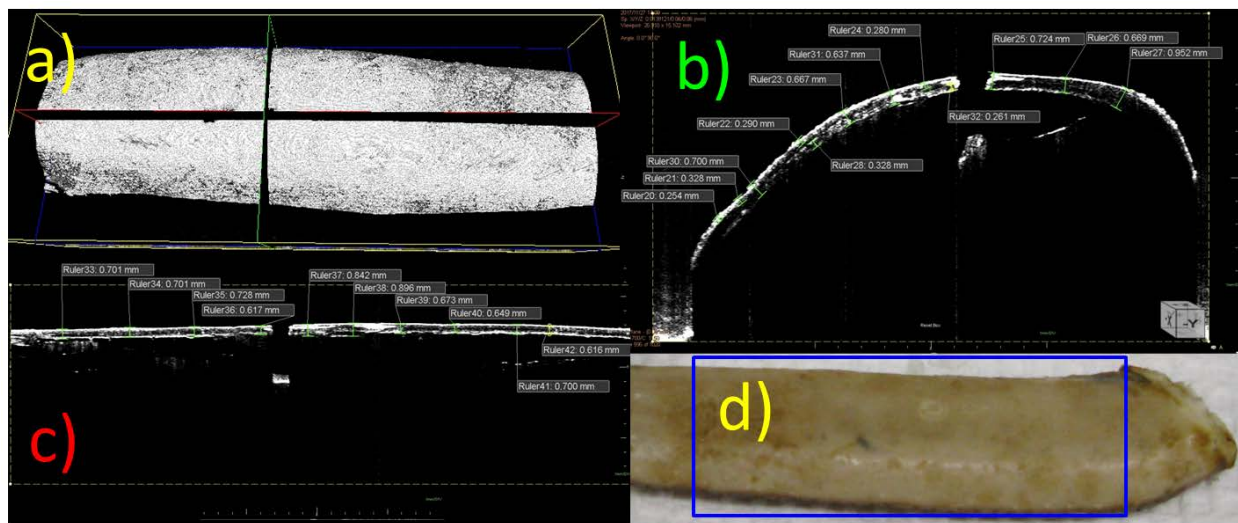


Figure 30 : (a) Tomographic reconstruction of (d) the merus of crab #5 (condition 3). (b, c) B-Scan reconstruction in the red and green planes of a) showing the shell thickness.

In crab #3 (Figure 31), multiple layers can be observed, but also a signal below that coming from a surface of soft tissue detached from the shell. This demonstrates that the system can see through the whole crab shell. The shell optical thickness is ranging from 600 to 800 μm .

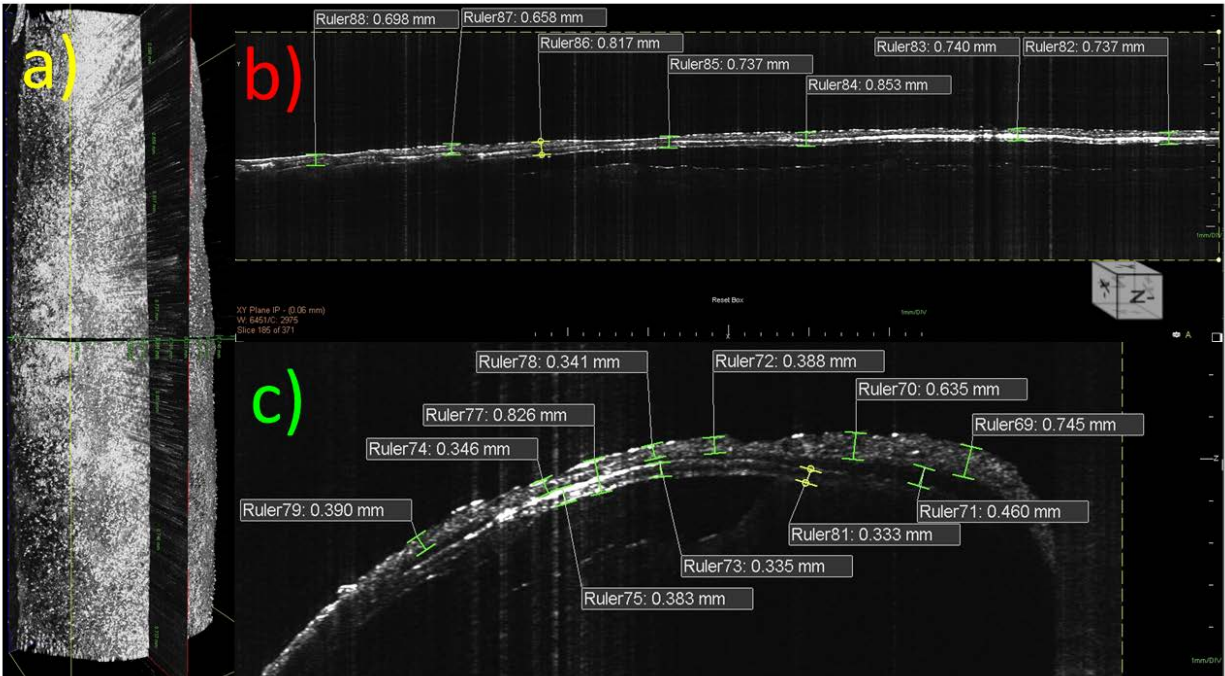


Figure 31 : (a) Tomographic reconstruction of the merus of crab #3 (condition 4).
(b, c) B-Scan reconstruction in the red and green planes of a) showing the shell thickness.

5.3.4 High resolution images

A few images of the Merus were also obtained with another slower OCT system, but with a higher resolution. As seen in Figure 32(a) and Figure 33(a), the structures at the surface of the shell appear with more details. The angle of the tomographic reconstruction in Figure 32(b) shows the continuity in the bright planes in the volume. It confirms again that the structure is a stack of layers. In crab #2 (Figure 32), the shell optical thickness is ranging from 900 to 1000 μm . In crab #3 (Figure 33), the shell optical thickness is ranging from 900 to 1200 μm .

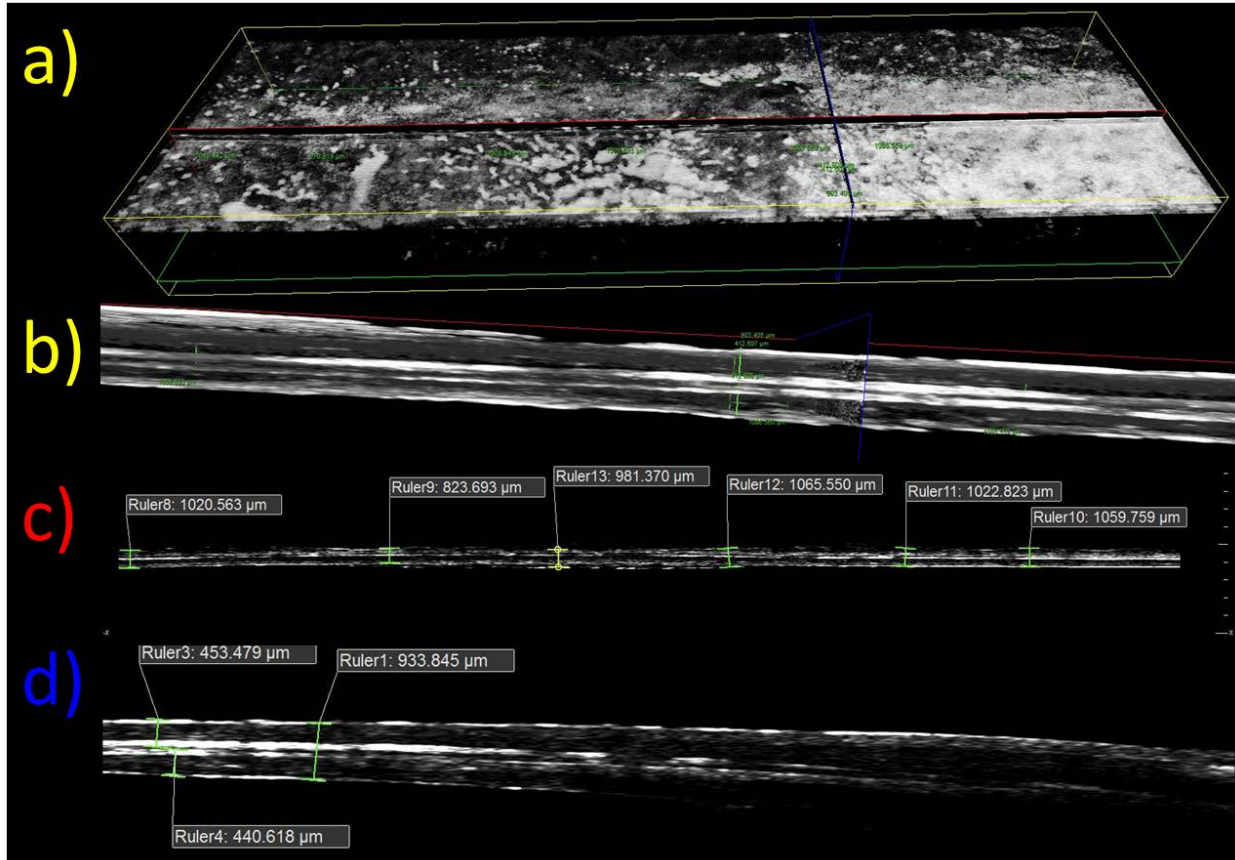


Figure 32 : (a, b) Tomographic reconstruction of the merus of crab #2 (condition 3M).
(c, d) B-Scan reconstruction in the red and blue planes of a) showing the shell thickness.

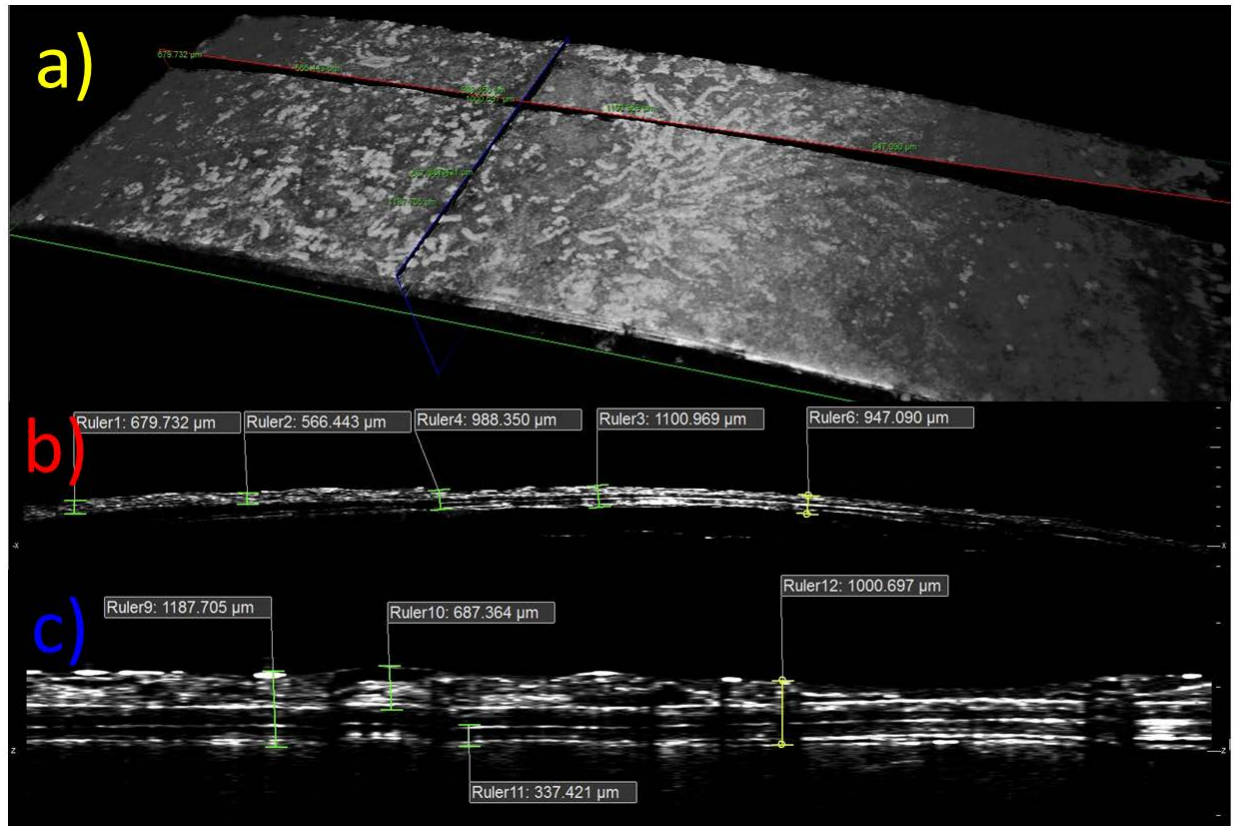


Figure 33 : (a) Tomographic reconstruction of the merus of crab #3 (condition 4). (b, c) B-Scan reconstruction in the red and blue planes of a) showing the shell thickness.

In conclusion, OCT imaging can quickly scan large areas of a crab shell and measure its optical thickness. It can see through the whole shell, since soft tissue interface could be observed underneath, without damaging it. Multiple layers stacked together could also be observed in the images obtained with the system and this information could probably be used by a trained specialist to draw conclusions and identify these different layers.

6. Ultrasounds Measurements

Ultrasonic waves can penetrate opaque materials and have been widely used in medical diagnostics and materials testing. In this section we report results on the evaluation of feasibility of ultrasound technique to characterize internal structure of snow crabs. Two areas have been of interest for the ultrasonic measurement on this report, the Cheliped of the Chela and the Merus of the 2nd Pereopod, because they are areas of smoother and softer surfaces where conventional ultrasonic transducers are easily applied.

6.1 Experimental

The classic pulse-echo ultrasonic technique was used. The ultrasonic transducer used is a Aerotech Alpha 2-15 MHz-0.25 that has a nominal frequency of 15 MHz that should be a good compromise for relatively thin layer characterization offering high resolution and acceptable attenuation. Lower and higher frequency transducers were also tested, but the 15 MHz presented better results. A delay line was used to better define echoes coming from interfaces close to the crab surface. Figure 34(a) shows a schematic view of the ultrasonic transducer with the delay line and the multiple echoes coming from the interfaces and Figure 34(b) shows a picture taken during a measurement.

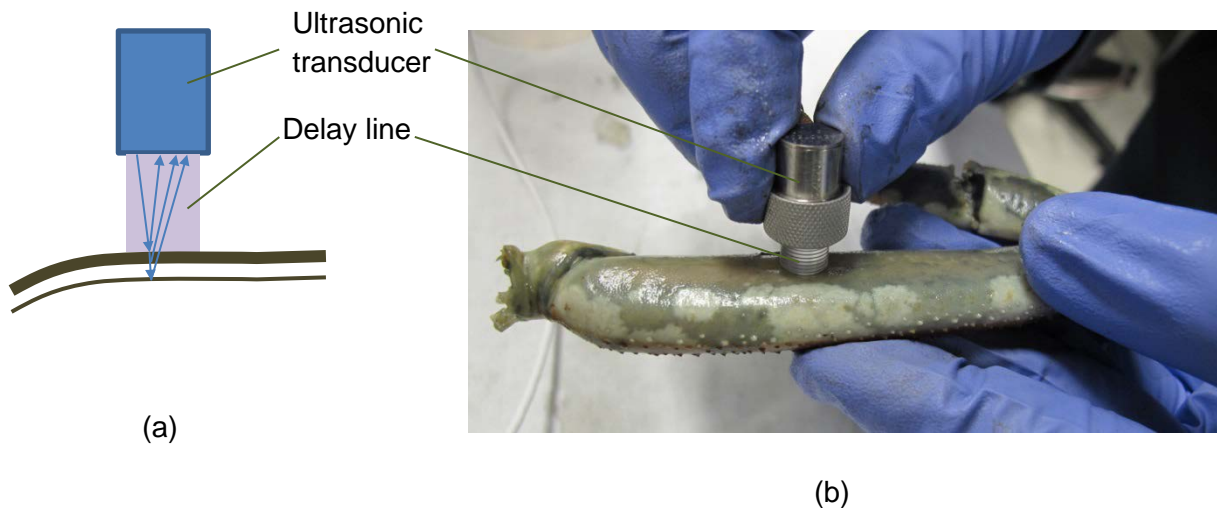


Figure 34 : (a) Schematic view of the ultrasonic transducer and the multiple echoes coming from the interfaces and (b) picture of the testing the merus of the 2nd pereopod.

6.2 Measurements

Figure 35 shows a signal obtained with the ultrasonic transducer and the delay line. The horizontal axis is the time in μs and the vertical axis is the voltage generated by the piezo element in the transducer. The echo that starts at about $8.3 \mu\text{s}$ is the echo reflected by the end of the delay line.

Figure 36 shows a signal when the transducer is in contact with one of the crab merus where other echoes coming from interfaces below the crab surface are visible. At least four echoes could be identified. The time of arrival of these echoes are proportional to the distance of the interface and the acoustic velocity. The acoustic velocity in water is close to 1.5 mm/ μ s. Bio tissues that have high water content tend to have acoustic velocity close to water. Osseous tissues tend to have higher acoustic velocity, typically on the 2-5 mm/ μ s range. The velocity is unknown for crab tissues and therefore only estimates of depth or thickness of the layers are possible.

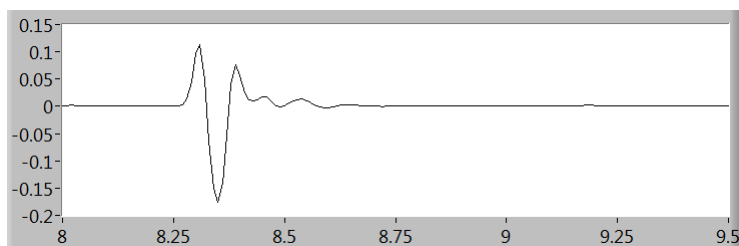


Figure 35 : Signal measured only with the delay line. Horizontal axis is the time in μ s and the vertical axis is the signal amplitude.

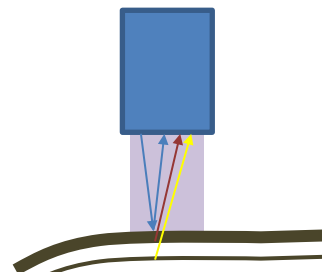
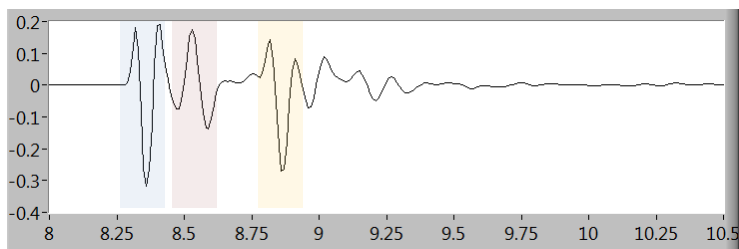


Figure 36 : Signal measured in the merus of the 2nd pereopod of crab #3.

The first echo shown in Figure 36 (blue) is from the delay line/crab shell interface. The next echo (brown), arriving about 0.2 μ s later, should be from the inner side of the shell. To determine the thickness of the shell, half of this time difference between the echoes should be multiplied by the acoustic velocity of the shell. If we take the range of velocity of osseous tissues (2-5 mm/ μ s) the thickness of the shell is in the range of 0.2 to 0.5 mm. This is in agreement with the measurements done by OCT that is in the 0.2-0.3 range (see Figure 30). The next echo (yellow) arrives at about 0.3 μ s later and if the velocity close to the water is assumed, the thickness of this layer is of about 0.2-0.25 mm. This seems to be lower than that measured by OCT in Figure 30, but it must be noted that the OCT measurement is an optical thickness that is not corrected by the diffraction index of the material.

Other echoes could be identified in Figure 36 and similar analysis could be applied. A measurement on another position in the merus, slightly different signals are obtained. Figure 37

shows another signal obtained in the same crab and part, but in a different measurement position. This signal illustrates well the variations related to different positions but also from the measurement technique itself that depends on the pressure applied on the transducer, its inclination, etc. But overall the same echoes identified in Figure 36 can be found in Figure 37.

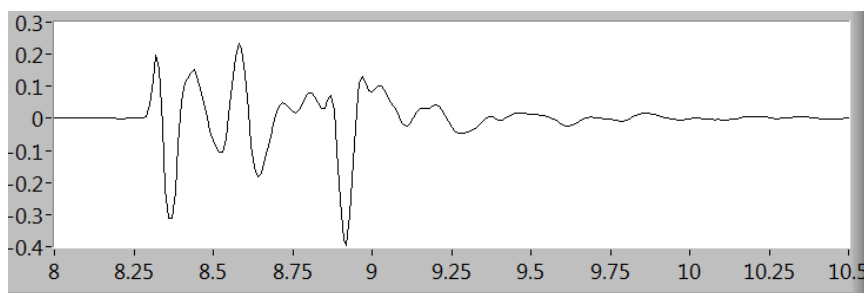


Figure 37 : Signal measured in the merus of the 2nd pereopod of crab #3 in other position than that shown in Figure 36.

6.3 Results

As mentioned earlier, the ultrasonic tests were performed in the Cheliped of the Chela and in the Merus of the 2nd Pereopod.

6.3.1 Cheliped of the Chela

The signals obtained in each crab are shown in Figure 38. As can be readily observed, the signals are clearly distinct for each crab condition. As the acoustic velocities are not known, quantitative analysis of the signals is not possible, but some features can be observed. Crab 2, for example only have echoes close to the first interface, while Crab 3 shows two clearly separated echoes. Note that the horizontal scale in Crab 3 has a delay, due to the use of a slightly longer delay line.

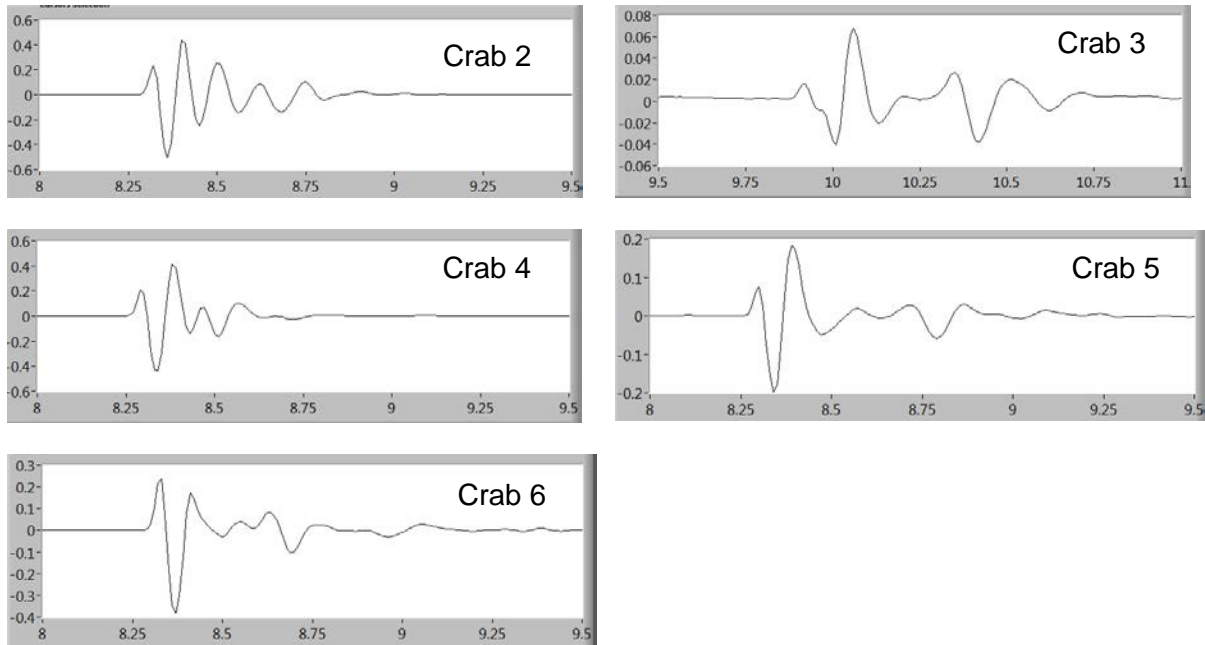


Figure 38 : Ultrasonic signals obtained on Cheliped of Chela from the tested crabs.

6.3.2 Merus of the 2nd pereopod

The ultrasonic signals for the tested crabs are shown in Figure 39. As for the Cheliped of the Chela, the signals are distinct for each crab. For example crab 4 shows only to close echoes, while other crabs have multiple echoes.

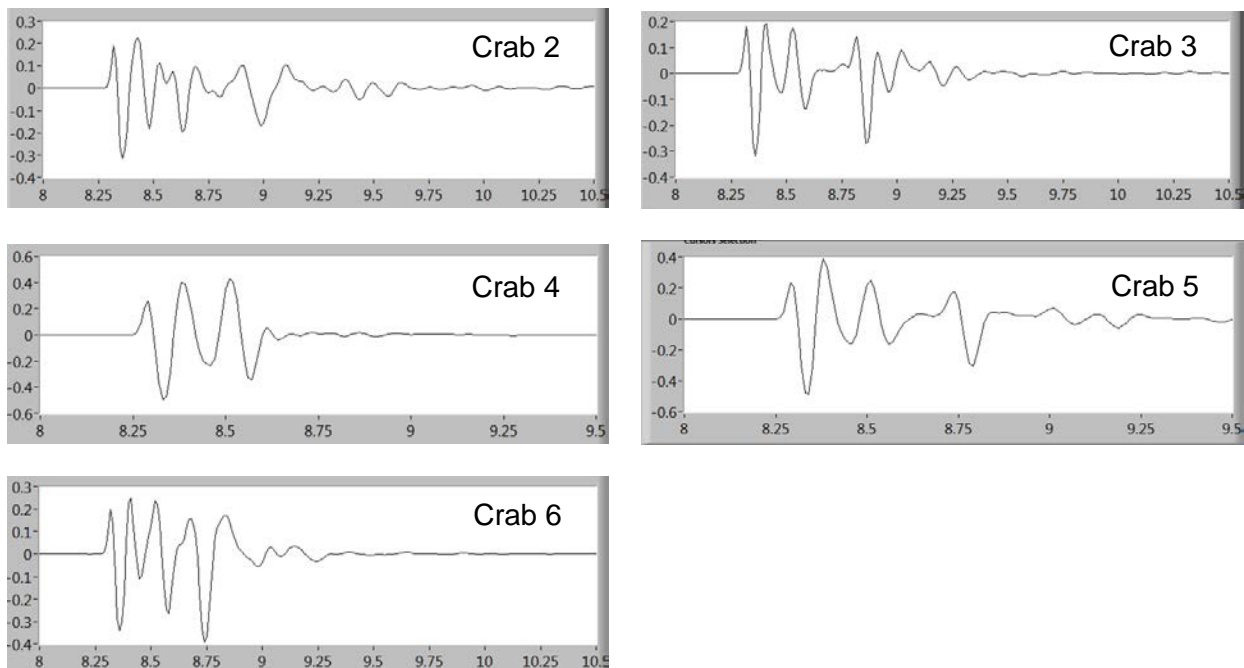


Figure 39 : Ultrasonic signals obtained on Merus of the 2nd pereopod from the tested crabs.

To conclude, the first remark of the ultrasonic results is that ultrasonic signals propagate well and present clear echoes with a very good signal-to-noise ratio. Second, while the measurements around the same position can present differences due to different pressure of the transducer, slightly different angle, couplant, etc., they present mostly the same signature. Third, the signals for different crabs presented clearly different signatures.

It is not straightforward to make the correlation between each crab condition and the signals observed. Although is easily observable, for example, that crab 2 which is in an immature condition presents a very distinct signal signature compared to the other crabs, as shown in Figure 39, the correlation with the actual tissue structure needs a more in-depth investigation. It would be interesting, for example, to follow the signal evolution a crab by taking multiple measurements on the same position along its moulting cycle, since the ultrasonic test is very quick and simple. Also, it would be interesting to have a better characterization of the acoustic velocities of different crab structures to be able to have quantitative description of the ultrasonic signals.

7. Conclusions and recommendations

LIBS, OCT and ultrasound measurements have been investigated to explore their applicability to characterized snow crabs shells. This study has provided the following points:

- The ability of LIBS applied to cheliped to distinguish postmoulters using the Mg/Ca ratios.
- The ability of LIBS applied to merus to distinguish postmoulters using the Mg(II)/Mg(I) ratios.
- The possibility to classify the different moulting stages using LIBS in combination with PCA.
- The ability of OCT imaging to quickly scan large areas of a crab shell and measure its optical thickness.
- The ability of OCT to “see” through the whole shell without damaging it.
- The ability of OCT to provide contrasts between the different layers composing the crab shell.
- Ultrasonic signal present clearly different fingerprints with a high signal to noise ratio, but correlation between crab condition and the signals needs more investigation.

LIBS, as a spectroscopic and multi-elemental method, has significant potential for applications using a portable sensor for crab identification. LIBS instruments could be deployed across a wide range of food and bio-based material applications. The capability of for rapid analysis makes LIBS a very useful sensor technology for sorting crabs. However, more investigations using a large number of snow crabs need to be performed in order to evaluate the robustness, the specificity and selectivity of the discrimination. Moreover, in order to avoid damaging the crab shell, other sampling strategies need to be studied to determine the minimum number of laser shots to perform a representative measurement. Other multivariate approaches such as soft independent modelling of class analogy (SIMCA), partial least squares discriminant analysis (PLS-DA) and support vector machines (SVM) also need to be investigated when having a large set of samples.

OCT is a very efficient imaging modality for cross-sectional imaging of biological tissue. This technology can not only clearly differentiate moulting conditions based on the thickness of the shell; it also allows more precise differentiation by providing a detailed imaging of the inner structure of the shell. A follow-up study would allow to better relate the structures observed in this report to the structures of the crab shell. Such a study could also aim at measuring the refractive index of the different layers, so optical thicknesses could be converted to geometrical thicknesses. Based on these studies, the specifications of an ideal OCT system could be determined, system which could be built in a further project. OCT systems can perform measurements at a high rate (50 000 depth profiles per second and more) so a whole crab can be imaged in less than one minute. OCT systems can be customized and specialized in many aspects. For example, an OCT system could be fabricated with a dynamic focus to provide high resolution imaging over the whole crab shell. NRC has expertise in developing OCT systems that are robust enough to be integrated in a manufacturing environment, an OCT system could thus even be fabricated to be used on a boat.

Regarding the ultrasound measurements, it can be stated that the technique has high potential to characterize crab structure in a very practical way, as the equipment is inexpensive, robust and easy to use. However, further investigation is necessary to better understand the correlation between the ultrasonic signals and actual crab shell structure.

Overall, LIBS and OCT are promising; however this report has only explored the applicability of those techniques and has not made an exhaustive assessment of each tool. It is recommended that the further investigations cited above be conducted to properly evaluate the capabilities of each or a combination of both techniques to fulfill the requirements of DFO in terms of functionality, portability and cost.

8. References

1. J. E. Sansonetti, W.C.M.a.S.L.Y., *Handbook of Basic Atomic Spectroscopic Data*. 2005.
2. Abdel-Salam, Z.A., et al., *Estimation of calcified tissues hardness via calcium and magnesium ionic to atomic line intensity ratio in laser induced breakdown spectra*. Spectrochimica Acta Part B: Atomic Spectroscopy, 2007. **62**(12): p. 1343-1347.
3. Singh, V.K., V. Kumar, and J. Sharma, *Importance of laser-induced breakdown spectroscopy for hard tissues (bone, teeth) and other calcified tissue materials*. Lasers in Medical Science, 2015. **30**(6): p. 1763-1778.
4. Alvira, F.C., F.R. Rozzi, and G.M. Bilmes, *Laser-Induced Breakdown Spectroscopy Microanalysis of Trace Elements in Homo Sapiens Teeth*. Applied Spectroscopy, 2010. **64**(3): p. 313-319.
5. Hausmann, N., et al., *Elemental mapping of Mg/Ca intensity ratios in marine mollusc shells using laser-induced breakdown spectroscopy*. Journal of Analytical Atomic Spectrometry, 2017. **32**(8): p. 1467-1472.
6. Garcia-Escarzaga, A., et al., *Mg/Ca ratios measured by laser induced breakdown spectroscopy (LIBS): a new approach to decipher environmental conditions*. Journal of Analytical Atomic Spectrometry, 2015. **30**(9): p. 1913-1919.
7. Wold, S., K. Esbensen, and P. Geladi, *Principal component analysis*. Chemometrics and intelligent laboratory systems, 1987. **2**(1-3): p. 37-52.
8. Barnes, R.J., M.S. Dhanoa, and S.J. Lister, *Standard Normal Variate Transformation and De-trending of Near-Infrared Diffuse Reflectance Spectra*. Applied Spectroscopy, 1989. **43**(5): p. 772-777.
9. Hebert, M., et al., *Moulting and Growth of Male Snow Crab, Chionoecetes opilio (O. Fabricius, 1788) (Decapoda, Majidae), in the Southern Gulf of St. Lawrence*. Crustaceana, 2002. **75**(5): p. 671-702.